Journal of Applied Mathematics and Physics, 2024, 12, 4242-4273
https://www.scirp.org/journal/jamp
ISSN Online: 2327-4379
ISSN Print: 2327-4352

MHD Nanofluid Flow Past a Vertical Plate Embedded in a Rotating Porous Medium with Chemical Reaction

Waheed A. Ahmed[1,2], Edward R. Onyango[3], David Theuri[3], Faiz Awad[4]

[1]Institute for Basic Sciences, Technology and Innovation, Pan African University, Nairobi, Kenya
[2]Department of Mathematics, Faculty of Mathematical and Computer Sciences, University of Gezira, Wad Medani, Sudan
[3]Department of Pure and Applied Mathematics, Jomo Kenyatta University of Agriculture and Technology, Juja, Kenya
[4]Department of Mathematics, Omdurman Islamic University, Omdurman, Sudan
Email: edward.onyango@jkuat.ac.ke

How to cite this paper: Ahmed, W.A., Onyango, E.R., Theuri, D. and Awad, F. (2024) MHD Nanofluid Flow Past a Vertical Plate Embedded in a Rotating Porous Medium with Chemical Reaction. *Journal of Applied Mathematics and Physics*, **12**, 4242-4273.
https://doi.org/10.4236/jamp.2024.1212261

Received: November 15, 2024
Accepted: December 28, 2024
Published: December 31, 2024

Abstract

In this paper, the problem of an unsteady free convection of MHD nanofluid flow past a semi-infinite vertical rotating plate embedded in a porous medium subject to a first-order chemical reaction has been studied numerically. The fluid flow has been mathematically modelled under the assumption that the viscosity of the fluid is temperature dependent. The governing dimensional partial differential equations were transformed into their equivalence non-dimensional form using a suitable variable. The resulting nonlinear partial differential equations were solved numerically using the bivariate interpolated spectral relaxation method (BI-SRM). The impacts of our physical parameters on the velocity components, temperature, concentration, and axial components of the induced magnetic field, as well as skin friction, are investigated using graphical and tabular forms. This establishes that as the rotation parameter increases, the secondary velocity field is rising, however when the Reynolds magnetic number increases, the opposite pattern is demonstrated.

Keywords

Temperature-Dependent Viscosity, Variable Magnetic Field, Rotating Frame, Permeability, Bivariate Spectral Relaxation Method

1. Introduction

Nanofluids are a relatively new technology consisting of nanoparticles mixed into a base fluid. Particles used in such a type of fluid are so small that each one is between 1 and 100 nanometres in size, which is made up of metal oxides, carbon

nanotubes or other materials, while the base fluid is mainly a liquid such as water, oil or ethanol. This mixture forms a fluid with properties that are much more efficient than those of traditional fluids [1]. It was Choi [2] who first used the expression "nanofluid". Nanofluids are found to have a higher thermal conductivity compared to the pure fluid [3]. In particular, the higher thermal conductivity allows nanofluids to be used as efficient coolants in electronics and other heat-generating devices. Nanofluids can also be engineered to have specific electrical conductivity and energy storage properties. In the medical field, nanofluids are also being used as drug delivery systems that can target specific areas of the body, and this type of delivery system can significantly improve the effectiveness of treatments and reduce the side effects of drugs. Earliest studies in the field of nanofluid by [4]-[10].

Many researchers investigate the field of nanofluid, among them Salem [11] who studied the effects of variable viscosity, viscous dissipation and chemical reaction on heat and mass transfer. Hammed and Pop [12] studied the unsteady free convection flow of a nanofluid past a permeable semi-infinite plate in the presence of an applied magnetic field, theoretically. They have succeeded in approximating an analytical solution to the boundary layer equations by means of the perturbation method. Loganathan and Sangeetha [13] used the implicit finite difference method to analyse the augmentation of thermal conductivity and mass transfer rate across a semi-infinite vertical plate due to nanoparticles suspended in Williamson fluid. Ullah *et al.* [14] numerically studied the two-dimensional Oldroyd-B flow of a nanofluid past a stretching sheet using the finite element method, under the effects of magnetic, electrical and thermal radiation. In an important study, Krishna and Chamkha [15] used the perturbation approximation approach to study the unsteady free convective flow of nanofluids at room temperature over a moving vertical plate. The plate is immersed in a homogeneous porous medium under thermal buoyancy with a constant heat source and convective boundary conditions. Furthermore, Krishna and Chamkha [16] studied unsteady MHD convective rotating flow of a nanofluid past a permeable moving vertical plate with a constant heat source using the perturbation method. Riasat *et al.* [17] used nanofluid with multi-walled carbon nanotubes between two rotating discs in a Darcy-Forchheimer permeable medium subject to an induced magnetic field to improve thermal conductivity in squeezing 3D magnetohydrodynamic thin film flow. Maneengam *et al.* [18] carried out numerical study of the flow of a hybrid nanofluid within a corrugated porous cavity in the presence of a magnetic field using the generalised finite element technique. Abumandour *et al.* [19] investigated the effects of slip, temperature conditions, and porosity on nanoparticle fluid suspension as well as the thermal nanofluid behavior as it flowed within a stenotic artery. Utilizing a catheter and vertical orientation, they explored the role of magnetic fields both with and without their presence. Using the homotopy analysis method, Ur Rasheed *et al.* [20], successfully evaluated the mixed convective MHD Jeffrey nanofluid flow. The study was conducted in the presence of a

vertical stretchable cylinder with heat and radiation absorption effects. Hossain *et al.* [21] used the finite volume method to study the bio-nanofluid flow regimes in a real bifurcated artery. The study showed that the influence of a magnetic source induced gradual changes in the pressure and vorticity profiles. Several investigations on nanofluid properties and MHD flow are thoroughly detailed in the literature [22]-[29].

The coupling of heat and mass transfer through porous media has a wide range of applications in thermal engineering, physics, mechanical engineering and chemistry, such as the design and optimization of heating, cooling, ventilation and air conditioning systems in various buildings and industries. The rate of heat and mass transfer through porous materials is influenced by the physical properties of these materials, including thermal conductivity, density, volume, temperature, humidity, and others. Porous media refers to materials that possess interconnected pores, channels, or voids. Porous materials are characterized by their porosity, which is a measure of the interconnected voids in the material. The intricate dynamics of nanofluid flow in a rotating porous media is a challenging subject to comprehend. It often requires the application of advanced mathematical models and simulations to accurately predict the transport phenomena. Moreover, the interplay between the nanoparticles and the pore surfaces plays a crucial role in determining the flow behaviour of nanofluids in porous media. The use of porous media is very encouraging, as it provides new insights into optimising the flow of nanofluids, thereby improving the efficiency of heat transfer and facilitating the sustainable use of energy. Reddy *et al.* [30] studied an unsteady natural convective flow of a nanofluid through a porous medium in a rotating system with convective and diffusive boundary conditions. They have solved the governing equations analytically using the perturbation approach. Kumar & Sood [31] investigated the three-dimensional MHD nanofluid flow over a vertical surface embedded in a porous rotating system. The principles of homogeneous-heterogeneous chemical reaction are introduced simultaneously. The governing equations are converted to dimensionless form and solved explicitly using a finite difference approach. Reddy *et al.* [32] demonstrated MHD flow of Cu-water and Ag-water nanofluids with heat and mass transfer in the presence of chemical reaction, thermal radiation and partial slip through a porous medium. They used similarity variables to convert the governing equations into ordinary differential equations, which were then solved numerically using the finite element method. Rashid *et al.* [33] investigated the MHD hybrid nanofluid flow between two parallel spinning discs in present of joule heating and chemical reactions. They utilised the Matlab programme "bvp4c" to numerically solve the governing equations. Recently, Abd-Alla *et al.* [34] introduced heat and mass transfer analysis on MHD Jeffery fluid flow through a porous medium utilising a rotating frame with a chemical reaction. Recently, nanofluids flow through rotating porous media with or without chemical reaction investigated widely by [35]-[41].

Magnetohydrodynamics convective flows with simultaneous heat and mass

transfer influenced by chemical reactions occur in many natural and artificial transport systems for instance in scientific and technological areas. Such applications of this phenomenon can be found in chemical vapour deposition on surfaces, nuclear reactor cooling, the petroleum industries, power and cooling sectors. In addition, convective flows occur naturally in temperature variations, concentration differences or a mixture of the two; for example, in air currents, concentration differences in the water where flow is affected by these concentration differences. Elsewhere this type of flow, which takes place through a porous plate, is of crucial importance in various scientific and mechanical applications. This prompted several scholars [42]-[48] to do extensive study on heat and mass transport of MHD free convective flow of fluid past a rotating plate with chemical reaction under different conditions. Prabhakar Reddy & Makinde [49] investigated a heat and mass transfer on MHD free convection flow under the influence of a chemical reaction. Also, Krishna *et al.* [50] studied numerically the problem of unsteady MHD natural convective rotating flow of an incompressible electrically conducting viscous fluid past an infinite vertical moving porous surface using cubic Bsplines collocation method. Very recently, Ayub *et al.* [51] investigated the problem of free convection on rotational flow of viscous fluid over an extended plate with heat and mass transfer in the presence of a constant-magnitude magnetic field through a porous medium.

Due to its importance in heat and mass transfer in some types of fluid flow, variable viscosity has been widely studied, recently. In a study by Ali *et al.* [52], temperature-dependent viscosity, convective boundary conditions, thermo-diffusion, and radiation effects were all taken into consideration to analysed the problem of unsteady MHD nanofluid flow across a radially nonlinear stretching sheet. They used the variational finite element method to solve the governing equations. A numerical study was carried out by Khan *et al.* [53] to analysed the impact of the variable viscosity on the flow of a Casson nanofluid over non-linear stretching sheet with slip and convective boundary conditions. With the motivation from all of the above efforts on a fact, specialised literature investigation tolerates that the effects of temperature-dependent viscosity, an induced magnetic field, nanofluid fluid, natural convection flow with heat, and mass transfer in the presence of a first-order chemical reaction through a semi-infinite vertical rotating plate embedded in a porous medium have not yet been discussed. Therefore, the current study claims to extend the Prabhaker Reddy and Makinde [49] for it is limitation of considering unsteady MHD free convective flow past through vertical plate in presence of chemical reaction such that the current study offered advancements of adding more specific consideration of variable viscosity, induced magnetic field with viscous dissipation and Joule heating, rotating plate, porous media saturated in fluidity with Copper(Cu) nanoparticles. Then to obtain the problem solution the novel BI-SRM numerical approach [54] [55] was chosen because it convincingly demonstrated the best in terms of accuracy and convergence speed, and computational cost is lacking as a direct comparison with other established

numerical methods (e.g., finite element, finite difference).

2. Mathematical Formulation

Let us consider an unsteady MHD boundary layer flow of an incompressible nanofluid driven by a semi-infinite vertical rotating plate embedded in a porous medium subject to chemical reaction. A coordinate frame is selected in which *x*-axis runs vertically along the plate, the *y*-axis is normal to the plate and directed into the fluid zone, in which the z-axis is taken to be normal to the *xy*-plane. Assumed that the nanofluid is formed with non-magnetic nanoparticles and base liquid with the velocity $(u,0,w)$. Let $\mu_e(H_x,H,H_z)$ be the induced magnetic vector at the given point in the fluid. A homogeneous transverse magnetic field of intensity H is applied parallel to the *y*-axis and perpendicular to the plate. Together, the fluid and plate rotate about *y*-aixs with a constant angular velocity Ω in the anticlockwise direction. Initially ($t=0$), both the fluid and plate are kept at a constant temperature T_w where $T_w > T_\infty$ is for a heated plate and $T_w < T_\infty$ corresponding to a cooled plate. At a certain time $0 < t < t_c$, the temperature of the plate is growing up to $T_\infty + (T_w - T_\infty)\frac{t}{t_0}$ here t_0 is the characteristic time. Moreover, the distribution of species concentration over the plate is boosted to $C_\infty + (C_w - C_\infty)\frac{t}{t_0}$. It is assumed that a homogeneous chemical reaction of first order with uniform rate K_r between the diffusing species and the ambient fluid exists. Figure 1 shows the geometry of the flow problem. The boundary layer equations controlling the flow include the continuity, motion, energy, concentration, and induction under the using Boussinesq's standard approximation respectively:

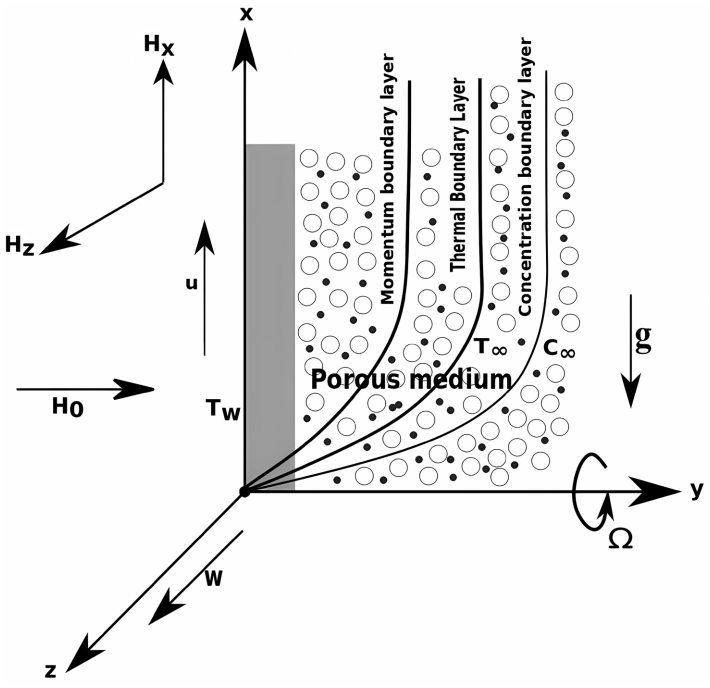

Figure 1. Physical model.

$$\frac{\partial u}{\partial x}+\frac{\partial w}{\partial z}=0, \tag{1}$$

$$\rho_{nf}\left(\frac{\partial u}{\partial t}+2\Omega w\right)=\frac{\mu_{nf}}{k}u+\frac{\partial}{\partial y}\left(\mu_{nf}\frac{\partial u}{\partial y}\right)+\sigma_{nf}\mu_e^2\left(\left(wH_x-uH_z\right)H_z-uH^2\right) + g\left(\rho\beta\right)_{nf}\left(T-T_\infty\right)+g\left(\rho\beta^*\right)_{nf}\left(C-C_\infty\right), \tag{2}$$

$$\rho_{nf}\left(\frac{\partial w}{\partial t}-2\Omega u\right)=\frac{\mu_{nf}}{k}w+\frac{\partial}{\partial y}\left(\mu_{nf}\frac{\partial w}{\partial y}\right)+\sigma_{nf}\mu_e^2\left(\left(uH_z-wH_x\right)H_x-wH^2\right), \tag{3}$$

$$\frac{\partial T}{\partial t}=\alpha_{nf}\frac{\partial^2 T}{\partial y^2}+\frac{\mu_{nf}}{\left(\rho C_p\right)_{nf}}\left(\frac{\partial u}{\partial y}\right)^2+\frac{\mu_{nf}}{\left(\rho C_p\right)_{nf}}\left(\frac{\partial w}{\partial y}\right)^2 + \frac{\sigma_{nf}\mu_e^2}{\left(\rho C_p\right)_{nf}}\left[H^2\left(w^2+u^2\right)+\left(wH_x-uH_z\right)^2\right], \tag{4}$$

$$\frac{\partial C}{\partial t}=D_m\frac{\partial^2 C}{\partial y^2}-k_r\left(C-C_\infty\right), \tag{5}$$

$$\frac{\partial H_x}{\partial t}=H\frac{\partial u}{\partial y}+\frac{1}{\sigma_{nf}\mu_e}\frac{\partial^2 H_x}{\partial y^2}, \tag{6}$$

$$\frac{\partial H_z}{\partial t}=-H\frac{\partial w}{\partial y}+\frac{1}{\sigma_{nf}\mu_e}\frac{\partial^2 H_z}{\partial y^2}, \tag{7}$$

where u and w represents the velocity components in the x and z directions, respectively, t is the time, T_w and C_w are the wall-dimensional temperatures and concentrations, respectively, T_∞ and C_∞, respectively are the free stream's starting temperature and concentration, ρ_{nf} is the nanofluid density, μ_{nf} is the nanofluid dynamic viscosity, σ_{nf} is the nanofluid electrical conductivity, α_{nf} is the nanofluid thermal diffusivity, T is the dimensional temperature, C is the dimensional mass concentration, C_{pnf} is the specific heat of the nanofluid at constant pressure, g is the gravitational acceleration, β_{nf} and β^* are the nanofluid thermal and concentration expansion coefficients respectively, μ_e and k are the magnetic and porous plate permeabilities respectively, K_r stands for the chemical reaction parameter.

The problem's initial boundary conditions are similar to those of Prabhaker Reddy and Makinde [49], and are presented as follows

$$\begin{aligned}
&u=0,w=0,T=T_\infty \text{ for all } L\geq y\geq 0 \text{ and } t=0,\\
&C=C_\infty,H_x=0,H_z=0 \text{ for all } L\geq y\geq 0 \text{ and } t=0,\\
&u=u_0,w=0,H_x=H,H_z=H \text{ at } y=0 \text{ for } t>0,\\
&T=T_\infty+\left(T_w-T_\infty\right)\frac{t}{t_0} \text{ when } 0<t\leq t_0 \text{ at } y=0 \text{ for } t>0,\\
&T=T_w \text{ when } t>t_0 \text{ at } y=0 \text{ for } t>0,\\
&C=C_\infty+\left(C_w-C_\infty\right)\frac{t}{t_0} \text{ when } 0<t\leq t_0 \text{ at } y=0 \text{ for } t>0,\\
&C=C_w \text{ when } t>t_0 \text{ at } y=0 \text{ for } t>0,\\
&u\to 0,w\to 0,H_x\to 0,H_z\to 0,T\to T_\infty,C\to C_\infty \text{ as } y\to\infty \text{ for } t>0.
\end{aligned} \tag{8}$$

where Initial velocity and time are u_0 and t_0, respectively. As a function of the nanoparticle, the following definitions for effective density, effective dynamic viscosity, thermal expansion coefficient, thermal diffusivity, heat capacitance, thermal conductivity, and electrical conductivity (see Minea [56], and Hamad & Pop [12]) are given, respectively:

$$\begin{aligned}
\rho_{nf} &= (1-\phi)\rho_f + \phi\rho_s, \\
\mu_{nf} &= \frac{\mu_f}{(1-\phi)^{2.5}}, \\
(\rho\beta)_{nf} &= (1-\phi)(\rho\beta)_f + \phi(\rho\beta)_s, \\
\alpha_{nf} &= \frac{\kappa_{nf}}{(\rho C_p)_{nf}}, \\
(\rho C_p)_{nf} &= (1-\phi)(\rho C_p)_f + \phi(\rho C_p)_s, \\
\frac{\kappa_{nf}}{\kappa_f} &= \frac{(\kappa_s + 2\kappa_f) - 2\phi(\kappa_f - \kappa_s)}{(\kappa_s + 2\kappa_f) + 2\phi(\kappa_f - \kappa_s)} \\
\sigma_{nf} &= \sigma_f\left[1 + \frac{3(\varepsilon-1)\phi}{(\varepsilon+2) - (\varepsilon-1)\phi}\right], \text{ where } \varepsilon = \frac{\sigma_s}{\sigma_f},
\end{aligned} \tag{9}$$

where ϕ denotes the volume of the nanoparticles that are made of solid material, ρ_f and ρ_s denote the densities of the fluid and solid particles, respectively, and β_s and β_f denote the coefficients of thermal expansion of the solid and fluid, respectively. The thermal conductivity of the base fluid and the solid are κ_f and κ_s, respectively, whereas the electrical conductivity of the fluid and the solid are σ_f and σ_s. **Table 1** lists the thermo-physical properties of the base fluid (water) and copper that are utilized for code validation.

Table 1. Base fluid and nanoparticle thermophysical properties.

Thermo-physical properties	Water	Copper (Cu)
Heat capacity $C_p\,(\mathrm{J/kg\cdot K})$	4179	385
Density $\rho\left(\mathrm{kg/m^3}\right)$	997.1	8933
Thermal conductivity $\kappa\left(\mathrm{W/m\cdot K}\right)$	0.613	400
Thermal expansion $\beta\times10^{-5}\left(1/\mathrm{K}\right)$	21	1.67
Electrical conductivity $\sigma\left(\Omega\cdot\mathrm{m}\right)^{-1}$	0.05	5.96×10^7

The fluid dynamic viscosity μ_f is considered to vary as an inverse function of temperature as given by Lai & Kulacki [57]:

$$\frac{1}{\mu_f} = \frac{1}{\mu_\infty}\left[1 + \gamma\left(T - T_\infty\right)\right]. \tag{10}$$

The transformation variables in dimensionless form are introduced as follows:

$$H_x^* = \frac{H_x}{H}, H_z^* = \frac{H_z}{H}; u^* = \frac{u}{u_0}, w^* = \frac{w}{u_0}$$
$$t^* = \frac{u_0 t}{L}, y^* = \frac{y}{L}; C^* = \frac{C - C_\infty}{C_w - C_\infty}; T^* = \frac{T - T_\infty}{T_w - T_\infty}. \tag{11}$$

Such that, Equations (2)-(7) can be written in the following dimensionless form (dropping asterisks):

$$\frac{\partial u}{\partial t} + 2Rw = a_1\left(K\frac{u}{1+\gamma\Delta TT} + \frac{1}{Re}\frac{\partial}{\partial y}\left(\frac{1}{1+\gamma\Delta TT}\frac{\partial u}{\partial y}\right)\right) + a_2 ReGrT + ReGmC + a_3 M\left(\left[wH_x - uH_z\right]H_z - u\right), \tag{12}$$

$$\frac{\partial w}{\partial t} - 2Rw = a_1\left(K\frac{w}{1+\gamma\Delta TT} + \frac{1}{Re}\frac{\partial}{\partial y}\left(\frac{1}{1+\gamma\Delta TT}\frac{\partial w}{\partial y}\right)\right) + a_3 M\left(\left[uH_z - wH_x\right]H_x - w\right), \tag{13}$$

$$\frac{\partial T}{\partial t} = a_4\left(\frac{1}{Re}\left[\frac{1}{Pr}\frac{\partial^2 T}{\partial y^2}\right]\right) + a_5\left(\frac{Ec}{Re}\frac{1}{1+\gamma\Delta TT}\left[\left(\frac{\partial u}{\partial y}\right)^2 + \left(\frac{\partial w}{\partial y}\right)^2\right]\right) + a_6\left(JeRe\left[\left(w^2+u^2\right) + \left(wH_x - uH_z\right)^2\right]\right), \tag{14}$$

$$\frac{\partial C}{\partial t} = \frac{a_7}{ScRe}\frac{\partial^2 C}{\partial y^2} - a_7 KcReC, \tag{15}$$

$$\frac{\partial H_x}{\partial t} = \frac{\partial u}{\partial y} + \frac{a_8}{Re_m}\frac{\partial^2 H_x}{\partial y^2}, \tag{16}$$

$$\frac{\partial H_z}{\partial t} = -\frac{\partial w}{\partial y} + \frac{a_8}{Re_m}\frac{\partial^2 H_z}{\partial y^2}. \tag{17}$$

Here $R = \frac{\Omega L}{u_0}$ is the Rotation parameter, $K = \frac{\mu_f L}{k\rho_f u_0}$ is the Permeability parameter, $Re = \frac{\rho_f u_0 L}{\mu_f}$ is the Reynolds number, $Gr = \frac{g\beta_f \nu_f \left(T_w - T_\infty\right)}{u_0^3}$ is the local temperature Grashof number, $Gm = \frac{g\beta^* \nu_f \left(C_w - C_\infty\right)}{u_0^3}$ is the local mass Grashof number, $M = \frac{\sigma_f \mu_e^2 H^2 L}{\rho_f u_0}$ is the Magnetic field parameter, $Pr = \frac{\mu_f Cp_f}{\kappa_f}$ is the Prandtl number, $Ec = \frac{u_0^2}{Cp_f \Delta T}$ is the Eckert number, $Je = \frac{\sigma_f \mu_e^2 H^2 \mu_f}{\rho_f^2 Cp_f \Delta T}$ is the Joule heating parameter, $Sc = \frac{\mu_f}{\rho_f D_m}$ is the Schmidt number, $Kc = \frac{k_r \mu_f}{\rho_f u_0^2}$ is the Chemical reaction parameter, $Re_m = \sigma_f \mu_e u_0 L$ is the Magnetic Reynolds number, $\Delta T = T_w - T_\infty$ is the temperature difference and where,

$$a_1 = \frac{(1-\phi)^{-2.5}}{(1-\phi)+\phi\rho_s/\rho_f},$$

$$a_2 = \frac{(1-\phi)+\phi(\rho\beta)_s/(\rho\beta)_f}{(1-\phi)+\phi\rho_s/\rho_f},$$

$$a_3 = \frac{(\epsilon+2)(1-\phi)+3\epsilon}{((\epsilon+2)-(\epsilon-1)\phi)((1-\phi)+\phi\rho_s/\rho_f)},$$

$$a_4 = \frac{(\kappa_s+2\kappa_f)-2\phi(\kappa_f-\kappa_s)}{((\kappa_s+2\kappa_f)+2\phi(\kappa_f-\kappa_s))((1-\phi)+\phi(\rho C_p)_s/(\rho C_p)_f)},$$

$$a_5 = \frac{(1-\phi)^{-2.5}}{(1-\phi)+\phi(\rho C_p)_s/(\rho C_p)_f},$$

$$a_6 = \frac{(\epsilon+2)(1-\phi)+3\epsilon}{((\epsilon+2)-(\epsilon-1)\phi)((1-\phi)+\phi(\rho C_p)_s/(\rho C_p)_f)},$$

$$a_7 = 1,$$

$$a_8 = \frac{(\epsilon+2)-(\epsilon-1)\phi}{(\epsilon+2)(1-\phi)+3\epsilon}.$$

The boundary conditions (8) in nondimensional form are

$$\begin{aligned}
&u=0, w=0, T=0, C=0, H_x=0, H_z=0 \text{ for all } 1\geq y\geq 0 \text{ and } t\leq 0,\\
&u=1, w=0, H_x=1, H_z=1 \text{ at } y=0 \text{ for } t>0,\\
&T=t \text{ when } 0<t\leq 1 \text{ at } y=0 \text{ for } t>0,\\
&T=1 \text{ when } t>1 \text{ at } y=0 \text{ for } t>0,\\
&C=t \text{ when } 0<t\leq 1 \text{ at } y=0 \text{ for } t>0,\\
&C=1 \text{ when } t>1 \text{ at } y=0 \text{ for } t>0,\\
&u\to 0, w\to 0, H_x\to 0, H_z\to 0, T\to 0, C\to 0 \text{ as } y\to\infty \text{ for } t>0.
\end{aligned} \tag{18}$$

Local skin friction coefficient:

The skin friction coefficient is a dimensionless quantity defined by the shear stress on the wall:

$$C_f = \frac{\tau_w}{\rho_{nf}u_0^2} \tag{19}$$

where ρ_{nf} and u_0 are the values of the nanofluid density and of the longitudinal velocity near the boundary layer's edge. Accordingly, at the plate with $y=0$, the primary and secondary shear stresses τ_x and τ_z are given by:

$$\tau_x = \mu_{nf}\left(\frac{\partial u}{\partial t}\right)_{y=0} \text{ and } \tau_z = \mu_{nf}\left(\frac{\partial w}{\partial t}\right)_{y=0}. \tag{20}$$

3. Numerical Method

This part is constructed to show the implementation of the Bivariate Spectral Relaxation Method (BI-SRM). The BI-SRM is a very effective tool that can be used

in solving the highly nonlinear differential equations. The BI-SRM, a relatively new technique, improves upon the Spectral Relaxation Method (SRM)(see Motsa *et al.* [58]), which is widely used for the numerical solution of the partial differential equations involved in the modeling of fluid flow. BI-SRM is introduced in this section in order to solve the system of the nonlinear partial differential Equations (12)-(17) along with the boundary conditions in (18). In order to make the spectral collocation method applicable, BI-SRM linearises the non-linear PDEs (12)-(17) to have

$$\alpha_1 \frac{\partial^2 u_{r+1}}{\partial y^2} + \alpha_2 \frac{\partial u_{r+1}}{\partial y} + \alpha_3 u_{r+1} - \frac{\partial u_{r+1}}{\partial t} = R_{u,r}, \tag{21}$$

$$\beta_1 \frac{\partial^2 w_{r+1}}{\partial y^2} + \beta_2 \frac{\partial w_{r+1}}{\partial y} + \beta_3 w_{r+1} - \frac{\partial w_{r+1}}{\partial t} = R_{w,r}, \tag{22}$$

$$\gamma_1 \frac{\partial^2 T_{r+1}}{\partial y^2} - \frac{\partial T_{r+1}}{\partial t} = R_{T,r}, \tag{23}$$

$$\sigma_1 \frac{\partial^2 C_{r+1}}{\partial y^2} + \sigma_2 C_{r+1} - \frac{\partial C_{r+1}}{\partial t} = R_{C,r}, \tag{24}$$

$$\delta_1 \frac{\partial^2 Hx_{r+1}}{\partial y^2} - \frac{\partial Hx_{r+1}}{\partial t} = R_{Hx,r}, \tag{25}$$

$$\omega_1 \frac{\partial^2 Hz_{r+1}}{\partial y^2} - \frac{\partial Hz_{r+1}}{\partial t} = R_{Hz,r}, \tag{26}$$

subject to

$$\begin{aligned}
&u_{r+1}(0,y) = 0,\ u_{r+1}(t,0) = 1;\ u_{r+1}(t,\infty) = 0,\\
&w_{r+1}(0,y) = 0,\ w_{r+1}(t,0) = 0;\ w_{r+1}(t,\infty) = 0,\\
&T_{r+1}(0,y) = 0,\ T_{r+1}(t,0) = 1;\ T_{r+1}(t,\infty) = 0,\\
&C_{r+1}(0,y) = 0,\ C_{r+1}(t,0) = 1;\ C_{r+1}(t,\infty) = 0,\\
&Hx_{r+1}(0,y) = 0,\ Hx_{r+1}(t,0) = 1;\ Hx_{r+1}(t,\infty) = 0,\\
&Hz_{r+1}(0,y) = 0,\ Hz_{r+1}(t,0) = 1;\ Hz_{r+1}(t,\infty) = 0.
\end{aligned} \tag{27}$$

The variable coefficients in above equations are determined by

$$\alpha_1 = \frac{a_1}{Re(1+\gamma\Delta TT_r)},\ \alpha_2 = \frac{a_1\gamma\Delta T}{Re(1+\gamma\Delta TT_r)^2}\frac{\partial T_r}{\partial y},$$

$$\alpha_3 = \frac{a_1 K}{1+\gamma\Delta TT_r} - a_3 M\left((Hz_r)^2+1\right),\ \beta_1 = \frac{a_1}{Re(1+\gamma\Delta TT_r)},$$

$$\beta_2 = \frac{a_1\gamma\Delta T}{Re(1+\gamma\Delta TT_r)^2}\frac{\partial T_r}{\partial y},\ \beta_3 = \frac{a_1 K}{1+\gamma\Delta TT_r} - a_3 M\left((Hz_r)^2+1\right),$$

$$\gamma_1 = \frac{a_4}{RePr},\ \sigma_1 = \frac{a_7}{ScRe},\ \sigma_2 = -a_7 KcRe,\ \delta_1 = \frac{a_8}{Re_m},\ \omega_1 = \frac{a_8}{Re_m},$$

$$R_{u,r} = 2Rw_r - a_2 ReGrT_r - ReGmC_{r+1} - a_3 M\left(w_r Hx_r Hz_r\right),$$

$$R_{w,r} = -2Ru_{r+1} - a_3 Mu_{r+1} Hz_r Hx_r,$$

$$R_{T,r} = -a_5 \frac{Ec}{Re\left(1+\gamma \Delta TT_r\right)}\left[\left(\frac{\partial u_{r+1}}{\partial y}\right)^2 + \left(\frac{\partial w_{r+1}}{\partial y}\right)^2\right]$$
$$- a_6 JeRe\left[\left(w_{r+1}^2 + u_{r+1}^2\right) + \left(w_{r+1}Hx_r - u_{r+1}Hz_r\right)^2\right],$$
$$R_{C,r} = 0,\ R_{Hx,r} = -\frac{\partial u_{r+1}}{\partial y},\ R_{Hz,r} = \frac{\partial w_{r+1}}{\partial y},$$

where $(r+1)$ and r denote the current and previous iterations, respectively. The Chebyshev spectral collocation is adopted to discretize the linear partial differential Equations (21)-(26) in both time (t) and space (y) directions. However, the spectral method is applicable only in the domain $[-1,1]$, due to this, we have to convert the physical domain of the problem from $(t,y) \in [0,1] \times [0, L_\infty]$ into $(\zeta,\eta) \in [-1,1] \times [-1,1]$ by suitable linear transformations. The linear partial differential Equations (21)-(26)) are decoupled, so each of them can be solved separately and their solutions can be approximated by a bivariate Lagrange polynomial standard form as follows:

$$U(\eta,\zeta) = \sum_{q=0}^{N_\zeta}\sum_{p=0}^{N_\eta} U\left(\eta_p,\zeta_q\right) L_p(\eta) L_q(\zeta), \tag{28}$$

$$W(\eta,\zeta) = \sum_{q=0}^{N_\zeta}\sum_{p=0}^{N_\eta} W\left(\eta_p,\zeta_q\right) L_p(\eta) L_q(\zeta), \tag{29}$$

$$T(\eta,\zeta) = \sum_{q=0}^{N_\zeta}\sum_{p=0}^{N_\eta} T\left(\eta_p,\zeta_q\right) L_p(\eta) L_q(\zeta), \tag{30}$$

$$C(\eta,\zeta) = \sum_{q=0}^{N_\zeta}\sum_{p=0}^{N_\eta} C\left(\eta_p,\zeta_q\right) L_p(\eta) L_q(\zeta), \tag{31}$$

$$H_x(\eta,\zeta) = \sum_{q=0}^{N_\zeta}\sum_{p=0}^{N_\eta} H_x\left(\eta_p,\zeta_q\right) L_p(\eta) L_q(\zeta), \tag{32}$$

$$H_z(\eta,\zeta) = \sum_{q=0}^{N_\zeta}\sum_{p=0}^{N_\eta} H_z\left(\eta_p,\zeta_q\right) L_p(\eta) L_q(\zeta), \tag{33}$$

To estimate variables in Equations (28)-(33) at predetermined points in the indicated directions η and ζ we introduce the Chebyshev-Gauss-Lobatto points

$$\left\{\eta_p\right\} = \left\{\cos\left(\frac{\pi p}{N_\eta}\right)\right\}_{p=0}^{N_\eta}, \left\{\zeta_q\right\} = \left\{\cos\left(\frac{\pi q}{N_\zeta}\right)\right\}_{q=0}^{N_\zeta}. \tag{34}$$

N_η and N_ζ, respectively, denote the number of grid points in the η and ζ directions. Additionally, the discrete derivatives at the grid points are obtained by transforming the continuous time and space derivatives using Chebyshev-Gauss-Lobatto (CGL) (34) grid points. Moreover, the common Lagrange cardinal polynomials cardinal polynomials $L_q(\eta)$ and $L_p(\zeta)$ are defined in the form

$$L_p(\eta) = \prod_{\substack{p=0 \\ p\neq s}}^{N_\eta} \frac{\eta - \eta_s}{\eta_p - \eta_s}, \tag{35}$$

where

$$L_p(\eta_s)=\delta_{ps}=\begin{cases}0 & \text{if } p\neq s,\\ 1 & \text{if } p=s.\end{cases} \tag{36}$$

The definition of the function $L_q(\zeta)$ is identical to that of the function $L_p(\zeta)$. Solution procedure starts by the determination of the derivative of $L_p(\eta)$ and $L_q(\zeta)$ with respect to η and ζ, therefore, calculating the Chebyshev partial derivative of $U(\eta,\zeta)$ with respect to ζ at any point (η_i,ζ_j) is given by

$$\left.\frac{\partial U}{\partial \zeta}\right|_{(\eta_i,\zeta_j)}=\sum_{q=0}^{N_\zeta}\sum_{p=0}^{N_\eta}U(\eta_q,\zeta_q)L_p(\eta)\left.\frac{\mathrm{d}L_q(\zeta)}{\mathrm{d}\zeta}\right|_{(\eta_i,\zeta_j)} \tag{37}$$

$$=\sum_{q=0}^{N_\zeta}\sum_{p=0}^{N_\eta}U(\eta_p,\zeta_q)L_p(\eta_i)\frac{\mathrm{d}L_q(\zeta_j)}{\mathrm{d}\zeta} \tag{38}$$

$$=\sum_{q=0}^{N_\zeta}\bar{D}_{jq}U(\eta_i,\zeta_q)=\sum_{q=0}^{N_\zeta}\bar{D}_{jq}U_q. \tag{39}$$

When $j,q=0,1,\cdots,N_\zeta$, the "Chebyshev Differentiation Matrix" [59] is utilized to produce the matrix's elements $\bar{D}_{jq}$. Partial derivatives of $U(\eta,\zeta)$ with respect to η are derived similarly. Similarly, at (η_i,ζ_i) CGL points, the partial derivative with respect to the space variable η is app

$$\left.\frac{\partial U}{\partial \eta}\right|_{(\eta_i,\zeta_j)}=\sum_{q=0}^{N_\zeta}\sum_{p=0}^{N_\eta}U(\eta_p,\zeta_q)\left.\frac{\mathrm{d}L_p(\eta)}{\mathrm{d}\eta}L_q(\zeta)\right|_{(\eta_i,\zeta_j)} \tag{40}$$

$$=\sum_{p=0}^{N_\eta}U(\eta_p,\zeta_j)\frac{\mathrm{d}L_p(\eta_i)}{\mathrm{d}\eta} \tag{41}$$

$$=\sum_{p=0}^{N_\eta}D_{ip}U(\eta_p,\zeta_j)=[\boldsymbol{D}]\boldsymbol{U}_j, \tag{42}$$

where i is the index nodes of η and p is the index basis of η, such that

$$\boldsymbol{U}_j=\left[u(\eta_0,\zeta_j),u(\eta_1,\zeta_j),u(\eta_2,\zeta_j),\cdots,u(\eta_{N_\eta},\zeta_j)\right]^\top. \tag{43}$$

where $\top$ denotes the matrix transpose. Consequently, the derivative of second order with respect to η is given by

$$\left.\frac{\partial^2 U}{\partial \eta^2}\right|_{(\eta_i,\zeta_j)}=\boldsymbol{D}^2\boldsymbol{U}_j. \tag{44}$$

Differentiation matrices of other dependent variables W,T,C,Hx,Hz are approximated by collocation, similar to Equations (39) and (42). Using the equations (39), (42) and (44) in Equation (24) we arrive at

$$\left[\sigma_1\boldsymbol{D}^2+\sigma_2\boldsymbol{I}\right]C_i-\sum_{q=0}^{N_\zeta}\bar{D}_{ij}\boldsymbol{U}_q=0,\ i=0,1,\cdots,N_\zeta. \tag{45}$$

According to the definitions of the dependent variables U,W,T,C,Hx,Hz and their derivatives, the Equations (21)-(26) can be written in the following

operator form

$$\left[\alpha_1 \boldsymbol{D}^2 + \alpha_2 \boldsymbol{D} + \alpha_3 \boldsymbol{I}\right] U_i - \sum_{j=0}^{N_\zeta - 1} \bar{D}_{ij} U_j = R_{u,i} \tag{46}$$

$$\left[\beta_1 \boldsymbol{D}^2 + \beta_2 \boldsymbol{D} + \beta_3 \boldsymbol{I}\right] W_i - \sum_{j=0}^{N_\zeta - 1} \bar{D}_{ij} W_j = R_{w,i}, \tag{47}$$

$$\gamma_1 \boldsymbol{D}^2 T_i - \sum_{j=0}^{N_\zeta - 1} \bar{D}_{ij} T_j = R_{T,i}, \tag{48}$$

$$\left[\sigma_1 \boldsymbol{D}^2 + \sigma_2 I\right] \boldsymbol{C}_i - \sum_{q=0}^{N_\zeta} \bar{D}_{ij} \boldsymbol{U}_q = 0, \tag{49}$$

$$\delta_1 \boldsymbol{D}^2 Hx_i - \sum_{j=0}^{N_\zeta - 1} \bar{D}_{ij} Hx_i = R_{Hx,i}, \tag{50}$$

$$\omega_1 \boldsymbol{D}^2 Hz_i - \sum_{j=0}^{N_\zeta - 1} \bar{D}_{ij} Hz_i = R_{Hz,i}, \tag{51}$$

where

$$R_{u,i} = R_{u,r} + \boldsymbol{D}_{iN_\zeta} U_{N_\zeta}, \quad R_{w,i} = R_{w,r} + \boldsymbol{D}_{iN_\zeta} W_{N_\zeta},$$

$$R_{T,i} = R_{T,r} + \boldsymbol{D}_{iN_\zeta} T_{N_\zeta}, \quad R_{C,i} = R_{C,r} + \boldsymbol{D}_{iN_\zeta} C_{N_\zeta},$$

$$R_{Hx,i} = R_{Hx,r} + \boldsymbol{D}_{iN_\zeta} Hx_{N_\zeta}, \quad R_{Hz,i} = R_{Hz,r} + \boldsymbol{D}_{iN_\zeta} Hz_{N_\zeta}.$$

Therefore, for $i = 0,1,\cdots,N_{\zeta-1}$, the boundary conditions in Equation (49) are established as in the following $N_\zeta\left(N_\eta+1\right)\times N_\zeta\left(N_\eta+1\right)$ matrix system:

$$\begin{bmatrix} Q_{0,0} & Q_{0,1} & \cdots & Q_{0,N_\zeta-1} \\ Q_{1,0} & Q_{1,1} & \cdots & Q_{1,N_\zeta-1} \\ \vdots & \vdots & \ddots & \vdots \\ Q_{N_\zeta-1,0} & Q_{N_\zeta-1,1} & \cdots & Q_{N_\zeta-1,N_\zeta-1} \end{bmatrix} \begin{bmatrix} \boldsymbol{C}_0 \\ \boldsymbol{C}_1 \\ \vdots \\ \boldsymbol{C}_{N_t-1} \end{bmatrix} = \begin{bmatrix} \boldsymbol{R}_{c,0} \\ \boldsymbol{R}_{c,1} \\ \vdots \\ \boldsymbol{R}_{c,N_{\zeta-1}} \end{bmatrix} \tag{52}$$

where

$$\begin{aligned} Q_{i,i} &= \sigma_1 \boldsymbol{D}^2 + \sigma_2 \boldsymbol{I} - \bar{D}_{ii} \boldsymbol{I} \\ Q_{i,j} &= -\bar{D}_{ij} \boldsymbol{I}, \ \text{when } i \neq j. \end{aligned} \tag{53}$$

The boundary condition (27) is imposed similarly for the remaining variables, and the bivariate Chebyshev collocation technique is performed similarly to produce

$$\left[\alpha_1 \boldsymbol{D}^2 + \alpha_2 \boldsymbol{D} + \alpha_3 \boldsymbol{I}\right] U_i - \sum_{j=0}^{N_\zeta - 1} \bar{D}_{ij} U_j = R_{u,i} \tag{54}$$

$$\left[\beta_1 \boldsymbol{D}^2 + \beta_2 \boldsymbol{D} + \beta_3 \boldsymbol{I}\right] W_i - \sum_{j=0}^{N_\zeta - 1} \bar{D}_{ij} W_j = R_{w,i} \tag{55}$$

$$\gamma_1 \boldsymbol{D}^2 T_i - \sum_{j=0}^{N_\zeta - 1} \bar{D}_{ij} T_j = R_{T,i} \tag{56}$$

$$\delta_1 \boldsymbol{D}^2 Hx_i - \sum_{j=0}^{N_\zeta - 1} \bar{D}_{ij} Hx_i = R_{Hx,i} \tag{57}$$

$$\omega_1 \boldsymbol{D}^2 Hz_i - \sum_{j=0}^{N_\zeta - 1} \bar{D}_{ij} Hz_i = R_{Hz,i} \tag{58}$$

The vectors U_{N_ζ}, W_{N_ζ}, T_{N_ζ}, C_{N_ζ}, Hx_{N_ζ} and Hz_{N_ζ} are the initial solutions derived from the supplied boundary conditions (27). After the boundary conditions are applied, Equations (54)-(58) are written as the following $N_\zeta\left(N_\eta+1\right)\times N_\zeta\left(N_\eta+1\right)$ matrices:

$$\begin{bmatrix} X_{0,0} & X_{0,1} & \cdots & X_{0,N_\zeta-1} \\ X_{1,0} & X_{1,1} & \cdots & X_{1,N_\zeta-1} \\ \vdots & \vdots & \ddots & \vdots \\ X_{N_\zeta-1,0} & X_{N_\zeta-1,1} & \cdots & X_{N_\zeta-1,N_\zeta-1} \end{bmatrix} \begin{bmatrix} \boldsymbol{U}_0 \\ \boldsymbol{U}_1 \\ \vdots \\ \boldsymbol{U}_{N_\zeta-1} \end{bmatrix} = \begin{bmatrix} \boldsymbol{R}_{u,0} \\ \boldsymbol{R}_{u,1} \\ \vdots \\ \boldsymbol{R}_{u,N_\zeta-1} \end{bmatrix} \tag{59}$$

$$\begin{bmatrix} Z_{0,0} & Z_{0,1} & \cdots & Z_{0,N_\zeta-1} \\ Z_{1,0} & Z_{1,1} & \cdots & Z_{1,N_\zeta-1} \\ \vdots & \vdots & \ddots & \vdots \\ Z_{N_\zeta-1,0} & Z_{N_\zeta-1,1} & \cdots & Z_{N_\zeta-1,N_\zeta-1} \end{bmatrix} \begin{bmatrix} \boldsymbol{W}_0 \\ \boldsymbol{W}_1 \\ \vdots \\ \boldsymbol{W}_{N_\zeta-1} \end{bmatrix} = \begin{bmatrix} \boldsymbol{R}_{w,0} \\ \boldsymbol{R}_{w,1} \\ \vdots \\ \boldsymbol{R}_{w,N_\zeta-1} \end{bmatrix} \tag{60}$$

$$\begin{bmatrix} F_{0,0} & F_{0,1} & \cdots & F_{0,N_\zeta-1} \\ F_{1,0} & F_{1,1} & \cdots & F_{1,N_\zeta-1} \\ \vdots & \vdots & \ddots & \vdots \\ F_{N_\zeta-1,0} & F_{N_\zeta-1,1} & \cdots & F_{N_\zeta-1,N_\zeta-1} \end{bmatrix} \begin{bmatrix} \boldsymbol{T}_0 \\ \boldsymbol{T}_1 \\ \vdots \\ \boldsymbol{T}_{N_\zeta-1} \end{bmatrix} = \begin{bmatrix} \boldsymbol{R}_{T,0} \\ \boldsymbol{R}_{T,1} \\ \vdots \\ \boldsymbol{R}_{T,N_\zeta-1} \end{bmatrix} \tag{61}$$

$$\begin{bmatrix} G_{0,0} & G_{0,1} & \cdots & G_{0,N_\zeta-1} \\ G_{1,0} & G_{1,1} & \cdots & G_{1,N_\zeta-1} \\ \vdots & \vdots & \ddots & \vdots \\ G_{N_\zeta-1,0} & G_{N_\zeta-1,1} & \cdots & G_{N_\zeta-1,N_\zeta-1} \end{bmatrix} \begin{bmatrix} \boldsymbol{Hx}_0 \\ \boldsymbol{Hx}_1 \\ \vdots \\ \boldsymbol{Hx}_{N_\zeta-1} \end{bmatrix} = \begin{bmatrix} \boldsymbol{R}_{Hx,0} \\ \boldsymbol{R}_{Hx,1} \\ \vdots \\ \boldsymbol{R}_{Hx,N_\zeta-1} \end{bmatrix} \tag{62}$$

$$\begin{bmatrix} P_{0,0} & P_{0,1} & \cdots & P_{0,N_\zeta-1} \\ P_{1,0} & P_{1,1} & \cdots & P_{1,N_\zeta-1} \\ \vdots & \vdots & \ddots & \vdots \\ P_{N_\zeta-1,0} & P_{N_\zeta-1,1} & \cdots & P_{N_\zeta-1,N_\zeta-1} \end{bmatrix} \begin{bmatrix} \boldsymbol{Hz}_0 \\ \boldsymbol{Hz}_1 \\ \vdots \\ \boldsymbol{Hz}_{N_\zeta-1} \end{bmatrix} = \begin{bmatrix} \boldsymbol{R}_{Hz,0} \\ \boldsymbol{R}_{Hz,1} \\ \vdots \\ \boldsymbol{R}_{Hz,N_\zeta-1} \end{bmatrix} \tag{63}$$

where

$$X_{i,i} = \alpha_{1,r}\boldsymbol{D}^2 + \alpha_{2,r}\boldsymbol{D} + \alpha_{3,r}\boldsymbol{I} - \bar{D}_{ii}\boldsymbol{I}, \quad X_{i,j} = -\bar{D}_{ij}\boldsymbol{I}, \text{ when } i \neq j,$$

$$Z_{i,i} = \beta_{1,r}\boldsymbol{D}^2 + \beta_{2,r}\boldsymbol{D} + \beta_{3,r}\boldsymbol{I} - \bar{D}_{ii}\boldsymbol{I}, \quad Z_{i,j} = -\bar{D}_{ij}I, \text{ when } i \neq j,$$

$$F_{i,i} = \gamma_{1,r}\boldsymbol{D}^2 - \bar{D}_{ii}\boldsymbol{I}, \quad F_{i,j} = -\bar{D}_{ij}\boldsymbol{I}, \text{ when } i \neq j,$$

$$G_{i,i} = \delta_{1,r}\boldsymbol{D}^2 - \bar{D}_{ii}\boldsymbol{I}, \quad G_{i,j} = -\bar{D}_{ij}\boldsymbol{I}, \text{ when } i \neq j,$$

$$P_{i,i} = \omega_{1,r}\boldsymbol{D}^2 - \bar{D}_{ii}\boldsymbol{I}, \quad P_{i,j} = -\bar{D}_{ij}\boldsymbol{I}, \text{ when } i \neq j,$$

$\boldsymbol{I}$ is the $\left(N_\eta+1\right)\times\left(N_\eta+1\right)$ unit matrix. The system of above matrices (59)-(63) is iteratively solved to get the numerical solution for $u(\eta,\zeta), w(\eta,\zeta), T(\eta,\zeta), Hx(\eta,\zeta)$ and $Hz(\eta,\zeta)$.

4. Results and Discussion

The results obtained by applying the Bivariate Spectral Relaxation Method (BI-SRM) to the problem of time-dependent MHD nanofluid flow driven by a semi-infinite vertical plate in a porous medium are carefully presented and thoroughly discussed in this section. As a check on the accuracy and convergent nature of the BI-SRM, we calculated the error of the method over orders see **Figure 2** and **Figure 3**. From these figures, it is observed that the BI-SRM achieves convergence in only 12 iterations with a maximum error of order 10^{-10} for the velocity and temperature profiles and 10^{-11} for both H_x, H_z of the induction profiles. To understand the physics of the problem, we have shown in **Figures 4-14** the effects of varying our governing parameters on velocity, temperature, concentration, induction fields as well as skin friction. Through all these figures, it is apparent that the mass volume fraction appearing leads to slowdown in the fluid motion. There are two potential explanations for this phenomenon. Firstly, it is worth

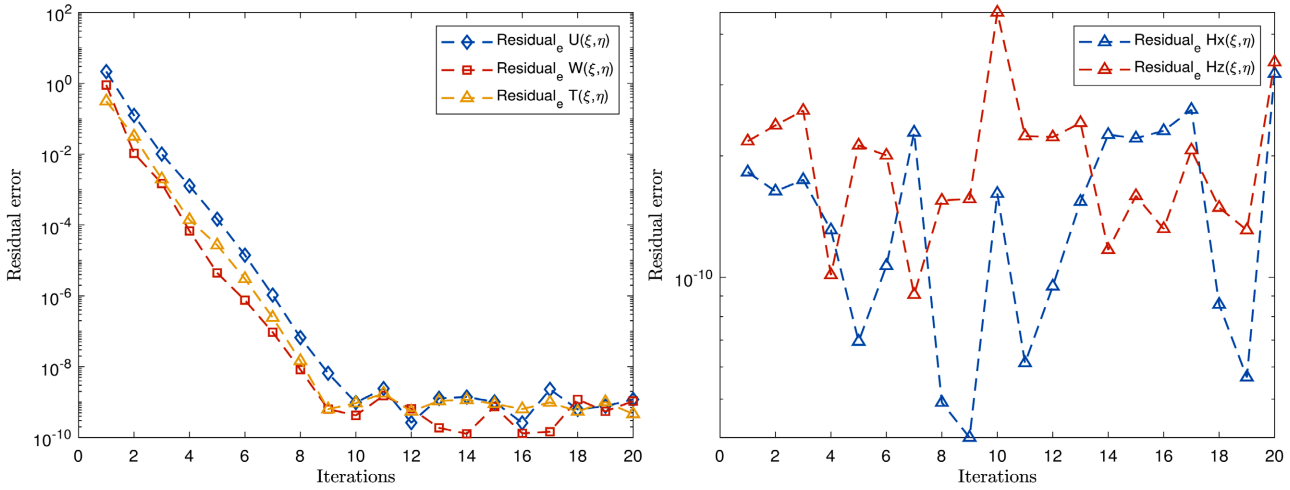

Figure 2. Residual error graphs.

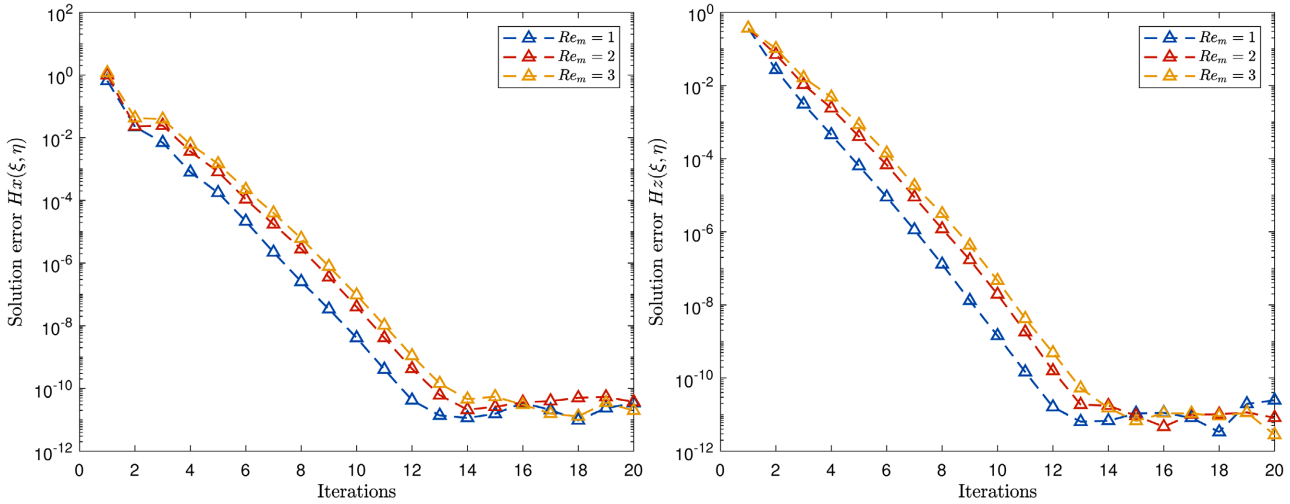

Figure 3. Solution error graphs.

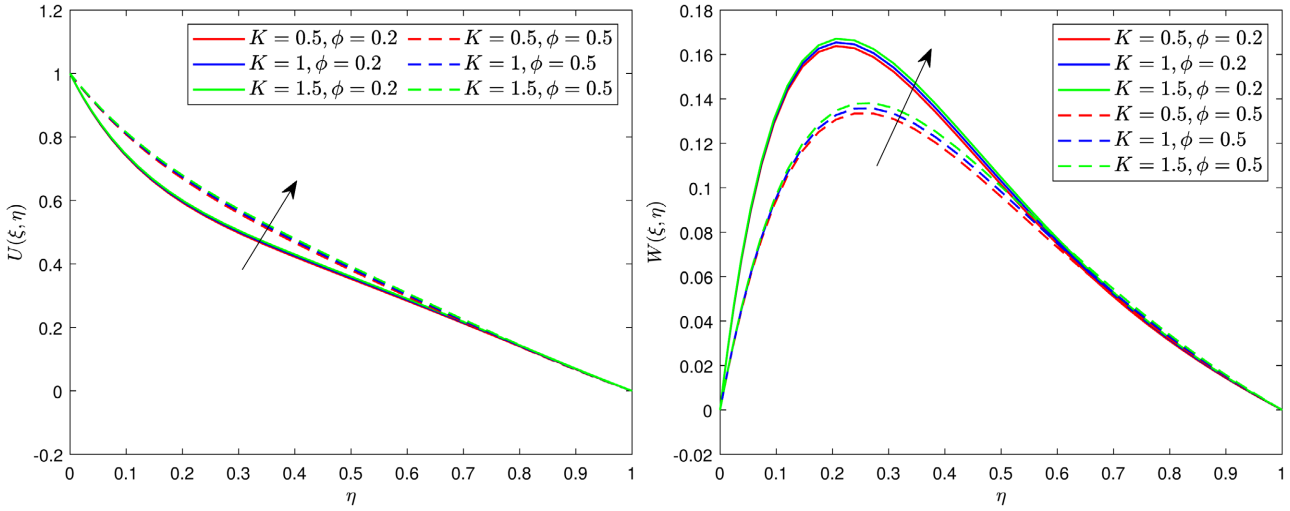

Figure 4. The velocity profiles for u and w against K and ϕ.

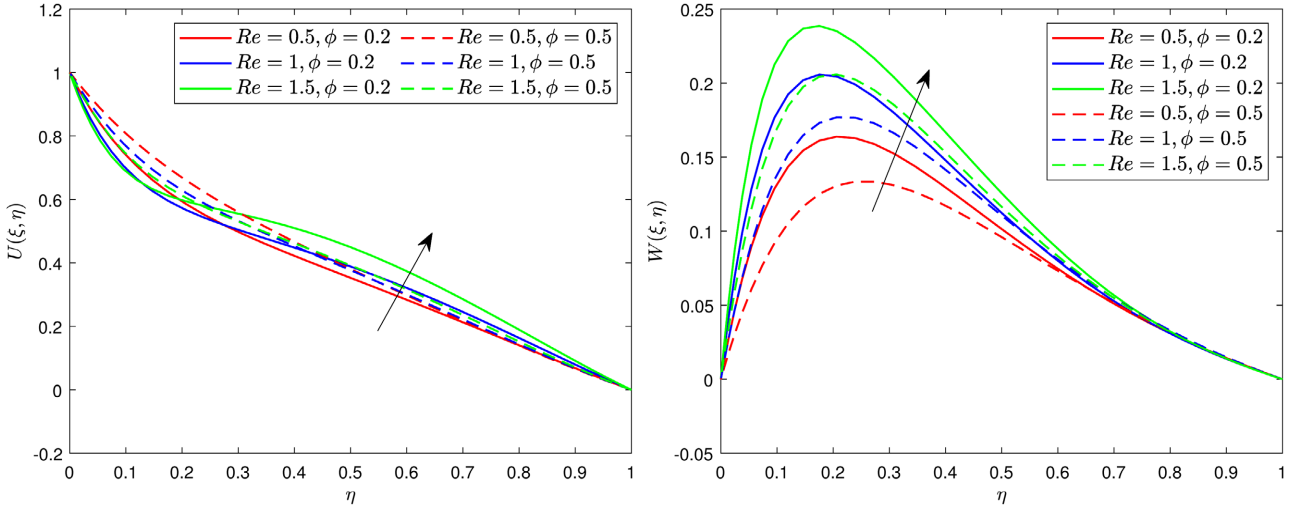

Figure 5. The velocity profiles for u and w against Re and ϕ.

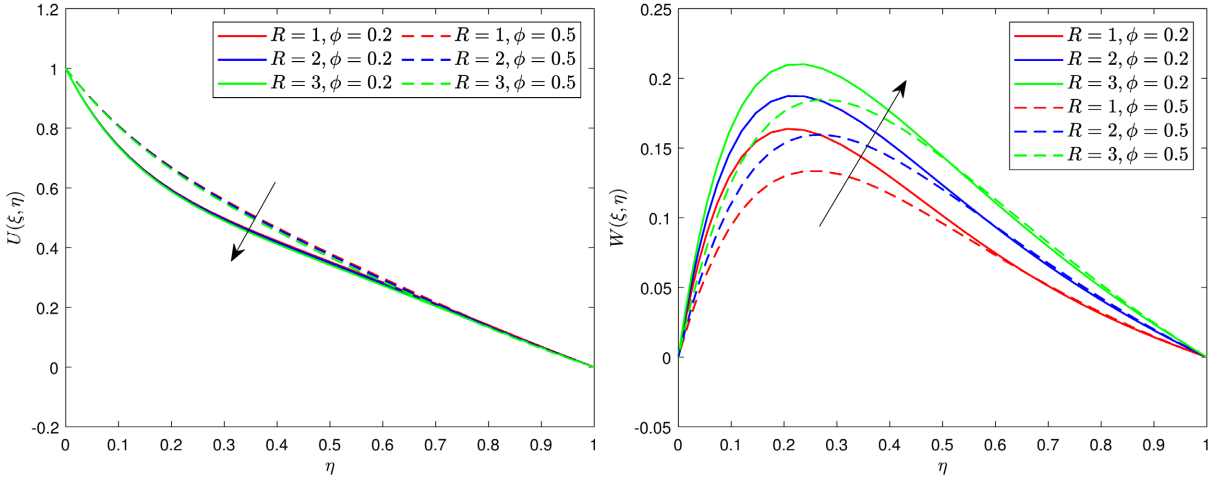

Figure 6. The velocity profiles for u and w against R and ϕ.

noting that larger nanoparticles undergo less Brownian motion, which increases resistance in the current and effectively reduces velocity. Secondly, raising nanoparticle concentration may increase fluid viscosity, thus causing a thicker momentum boundary layer, which could ultimately decelerate fluid motion.

The influence of permeability K of the porous media on the velocity profiles is displayed in Figure 4 for different values of nanoparticle volume fractions. It is observed that raising the permeability coefficient of the porous medium reduces the resistance between the fluid and medium, leading to a thinner momentum boundary layer, hence increasing the primary and secondary flow. Figure 5 shows the influence of the Reynolds number Re on the velocity components u and w. The Reynolds number relates the fluid momentum to the viscous shear stress in the fluid system. Increasing the Reynolds number decreases the ratio $1/Re$, causing the momentum force to become negligible compared to the viscous forces. This enhances the thickness of the momentum boundary layer so that the velocity components u and w increase as $1/Re$ decreases. See Fig. 6 for the effect of the rotation parameter R on the primary velocity u and the secondary velocity w. It is evident that as the rotation parameter R increases, the primary velocity u decreases. This phenomenon occurs due to the dominance of the Coriolis force exerted by the fluid medium in the direction of rotation. For the same reason, it is also worth noting that the secondary velocity increases with the rotation parameter. Figure 7 illustrates how the magnetic field M affects the primary and secondary velocity, respectively.

It can be seen that the primary flow velocity decreases significantly as the magnetic parameter M increases. In a particular case, secondary flow velocity increases near the plate as M increases and then decreases away from the plate as M increases. In practice, this occurs due to the Lorentz force created by the magnetic field which acts against the flow. Figure 8 and Figure 9 show the variations of the primary and secondary velocities with respect to the thermal Grashof number Gr and the concentration Grashof number Gm, which represent the ratio of the thermal and concentration buoyancy forces to the viscous force, respectively. As it is known that the thermal and concentration Grashof numbers increase, Gr and Gm increase the effectiveness of the thermal and concentration buoyancy forces, resulting in an increase in the thermal Grashof number, the mass Grashof number, or both, which increases the thickness of the momentum boundary layers, thus increasing the velocities.

Figure 10 shows the velocity profiles of the primary and secondary components, u and w, respectively, for different values of the Prandtl number Pr. In fact, the ratio $1/Pr$ is a decreasing function of Pr, so in our fluid case, increasing Pr causes highly viscous flow. Therefore, both velocity components increase with increasing Pr. Figure 11 illustrates the effect of the chemical reaction parameter on the velocity components u and w. The results indicate that increasing the chemical reaction parameter leads to a reduction in both primary and secondary velocities, this is due to a decrease in fluid concentration.

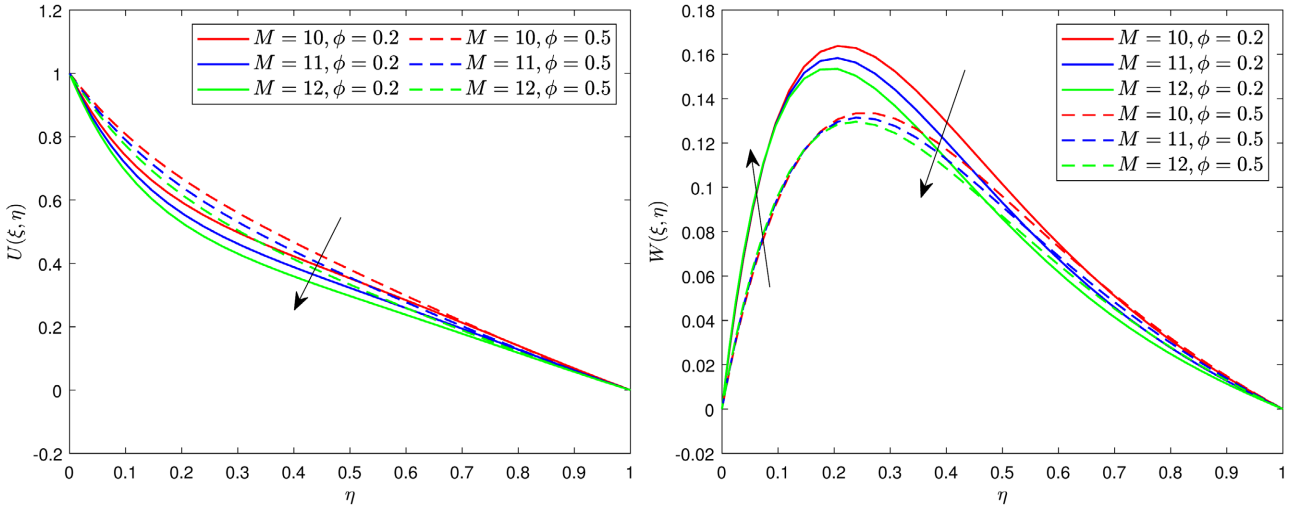

Figure 7. The velocity profiles for u and w against M and ϕ.

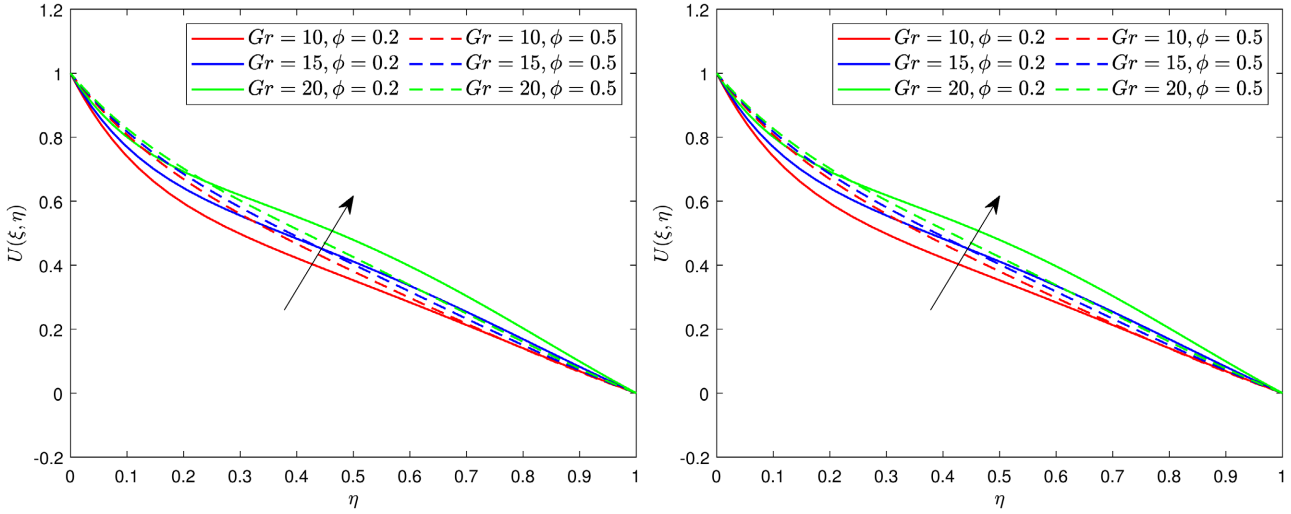

Figure 8. The velocity profiles for u and w against Gr and ϕ.

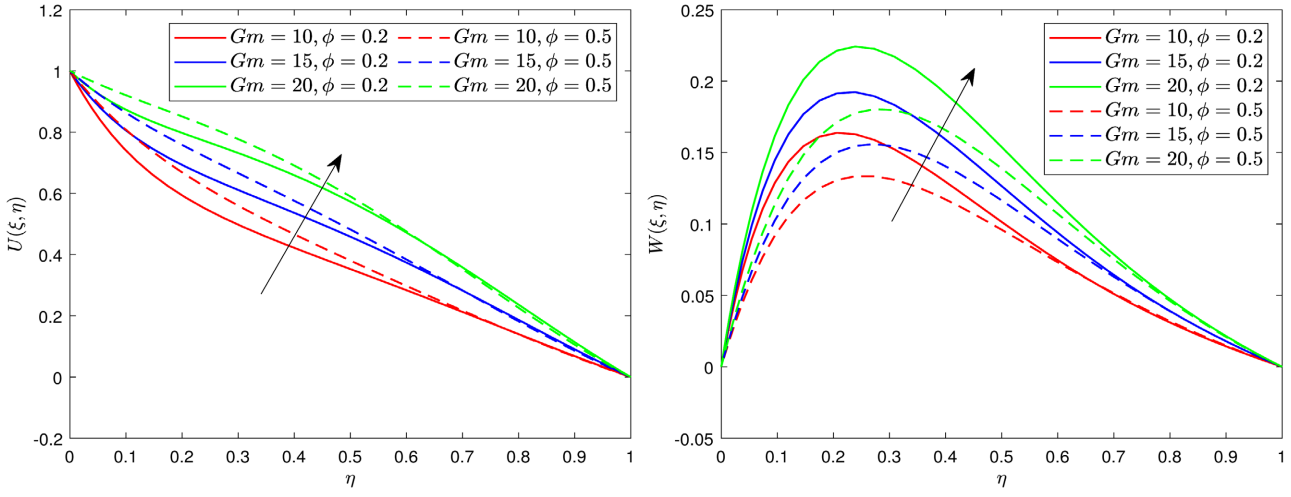

Figure 9. The velocity profiles for u and w against Gm and ϕ.

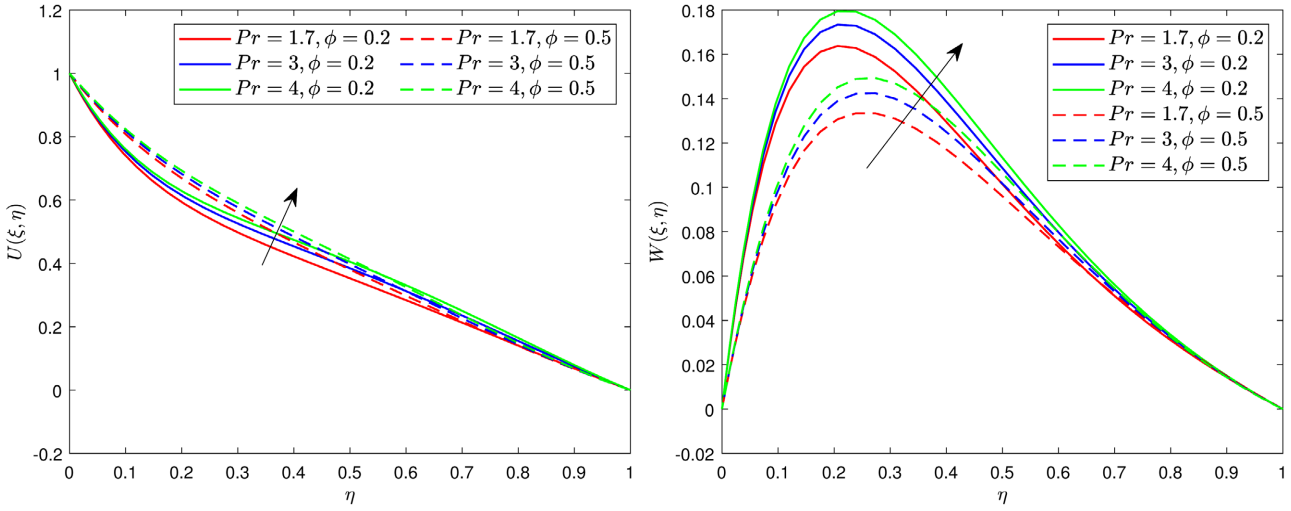

Figure 10. The velocity profiles for u and w against Pr and ϕ.

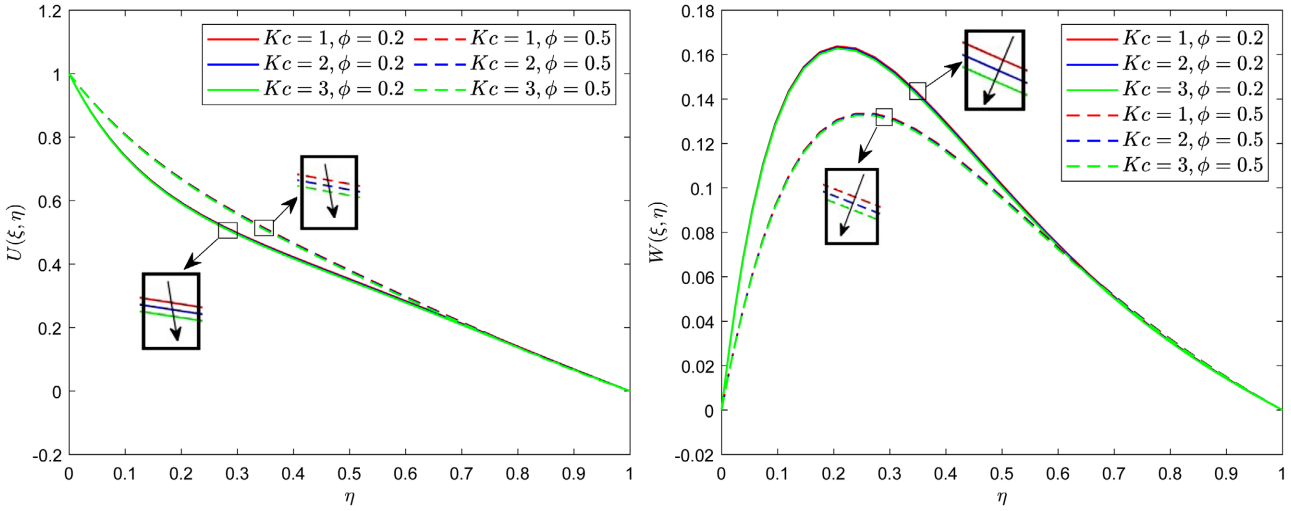

Figure 11. The velocity profiles for u and w against Kc and ϕ.

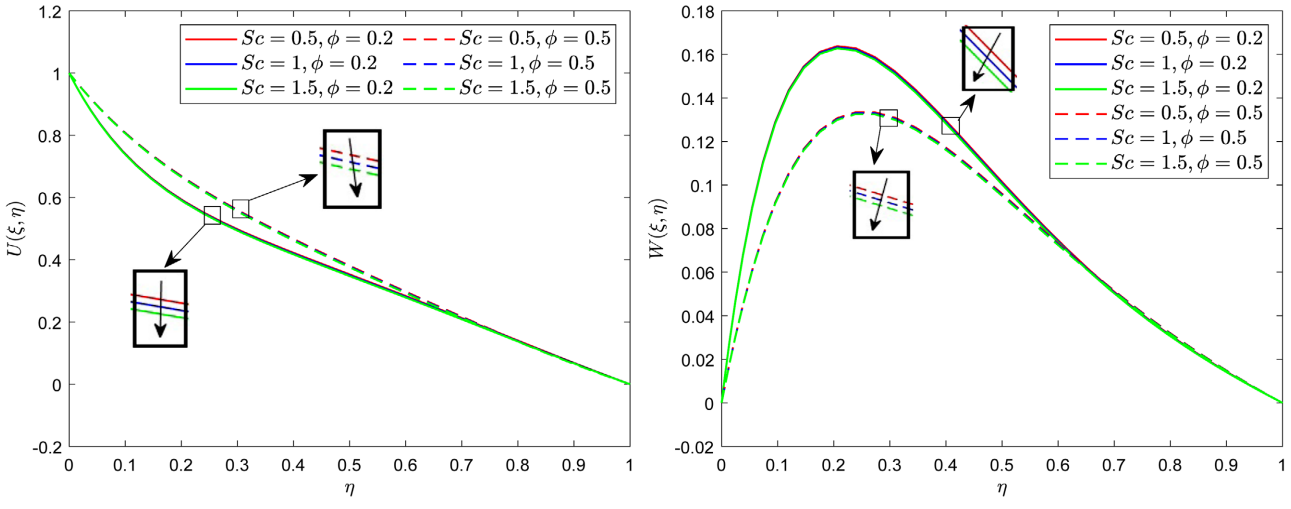

Figure 12. The velocity profiles for u and w against Sc and ϕ.

Figure 12 shows the effect of Schmidt number Sc on the primary and secondary velocity profiles. As Sc increases, both u and w tend to decrease. This is because an increase in Sc leads to a decrease in molecular diffusivity, resulting in a thicker momentum boundary layer. The fluid velocity then decreases in both directions.

The primary and secondary velocity patterns for different values of the Reynolds magnetic number (Re_m) which estimates the induction of magnetic diffusion by a magnetic field are plotted in Figure 13. Here is roughly estimated by the magnetic Reynolds number. As Re_m increases, the primary velocity rises, while the secondary speed decreases. Physically, an increase in Re_m leads to enhanced magnetic diffusion generates Lorentz drag, which interacts with fluid motion, resulting in a decrease in the primary velocity profile. Conversely, the secondary velocity exhibits the opposite trend for a while and then decreases due to the same indicated reasons. On the other hand, the side effects of the magnetic Reynolds number Re_m on both axially induced magnetic fields, Hx and Hz, are shown in Figure 14. It can be seen that both Hx

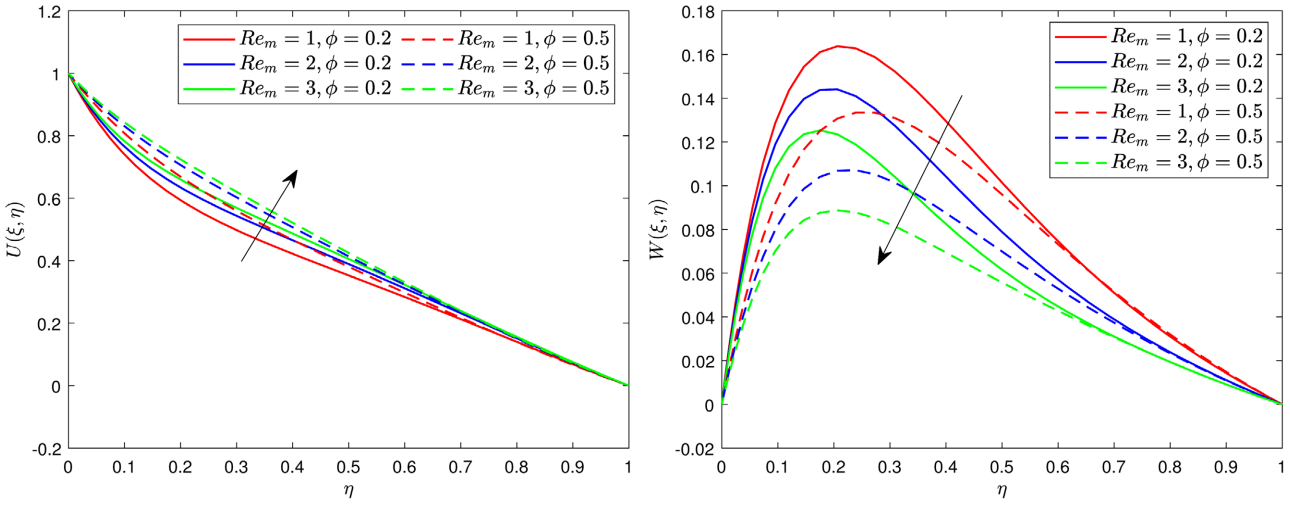

Figure 13. The velocity profiles for u and w against Re_m and ϕ.

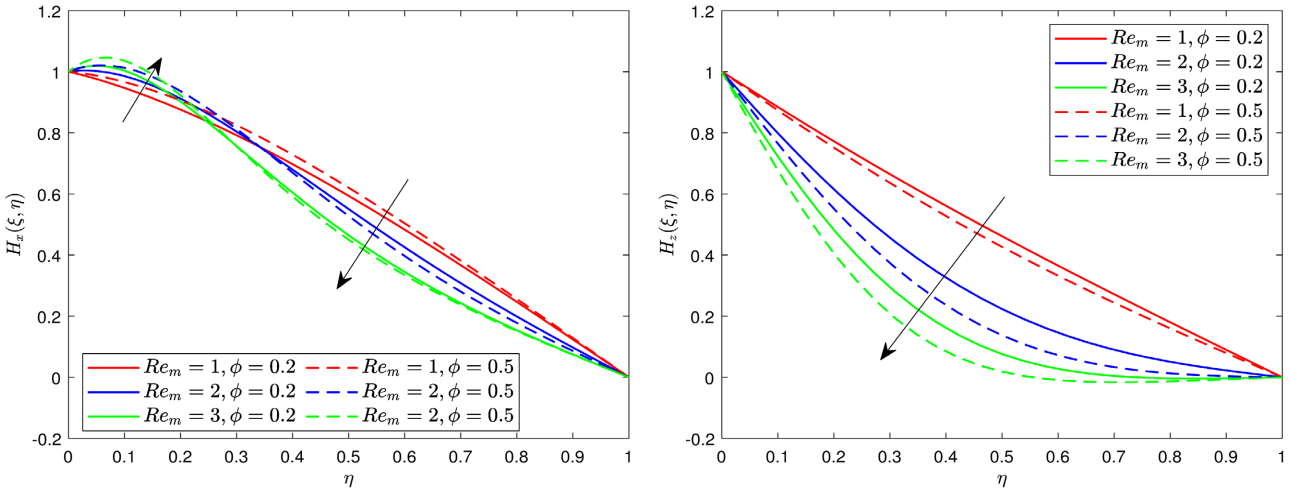

Figure 14. The magnetic profiles for Hx and Hz against Re_m and ϕ.

and Hz are decreasing functions in Re_m. This is because as Re_m decreases, the mass diffusivity increases and this accelerates the flow regime.

Figure 15 illustrates the temperature distribution for different values of Reynolds number Re and mass volume fraction ϕ. The figure shows that as the Reynolds number increases, the heat flux cells become smaller and smaller in size. An increasing Reynolds number indicates that the inertial forces become dominant compared to the viscous force. This causes the fluid to accelerate, as a result, more heat is transported by convection. It also can be seen that increasing the amount of mass volume fraction has a positive effect on the thermal conductivity of the system. Figure 16 and Figure 17 are plotted to illustrate the impacts of Schmidt number Sc and Prandtl number Pr on temperature distribution, respectively. From Figure 16, it is very noticeable that iso-thermal cells become an increasing function of Sc. This means that by increasing Sc, the temperature is well distributed over the flow area. Conversely, it is clear that from Figure 17, the effects of the Prandtl number on the temperature distribution is to produce a completely opposite behavior. For different values of the Schemdit number Sc at $Re = 2$ and $Re = 5$, the distribution of the concentration was plotted in Figure 18. We found that the concentration distribution is strongly time dependent near the edge of the plate. When both Sc and Re are increasing, the concentration occupies a narrow region of the solution domain. Figure 19 illustrates the effect of the Eckert number Ec in the temperature distribution field. It is seen that increasing of Ec enhances the temperature distribution over the region domain. This demonstrates how the Ec number plays a significant role in the temperature distribution.

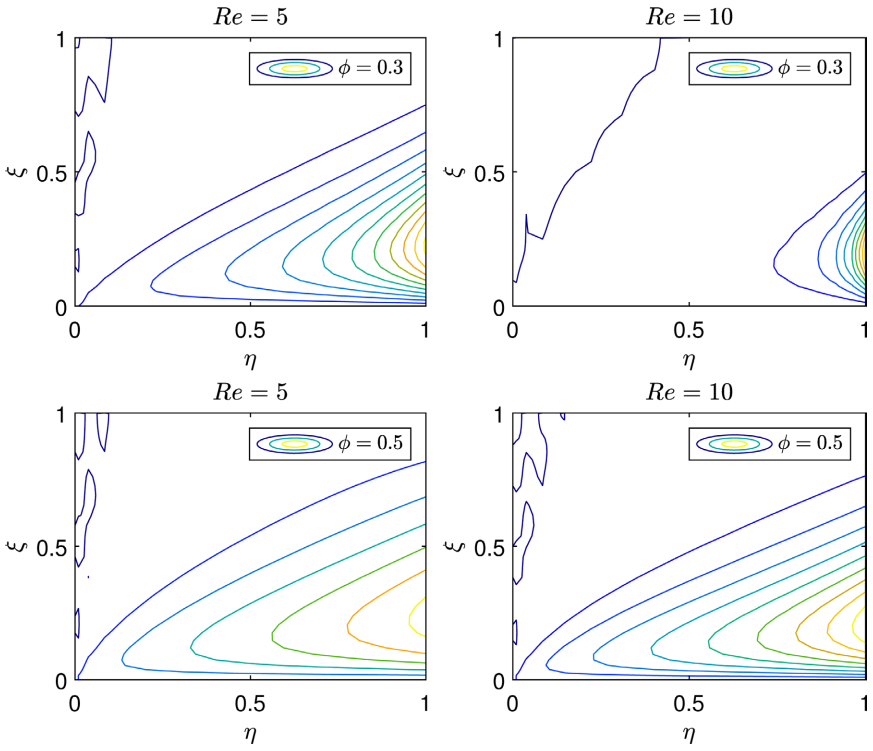

Figure 15. Temperature distribution for different values of Re and ϕ.

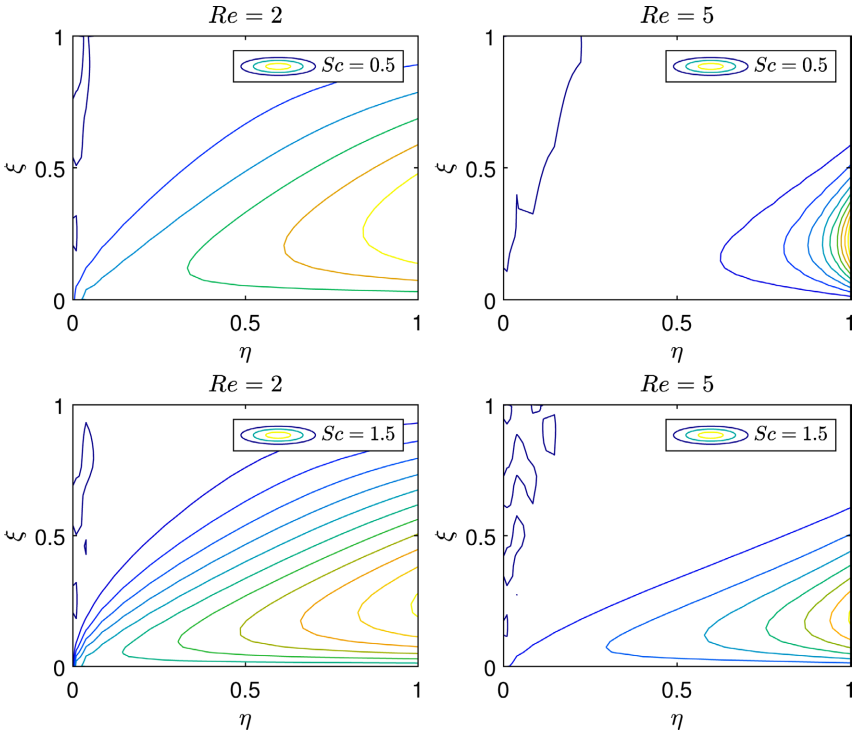

Figure 16. Temperature distribution for different values of *Re* and *Sc*.

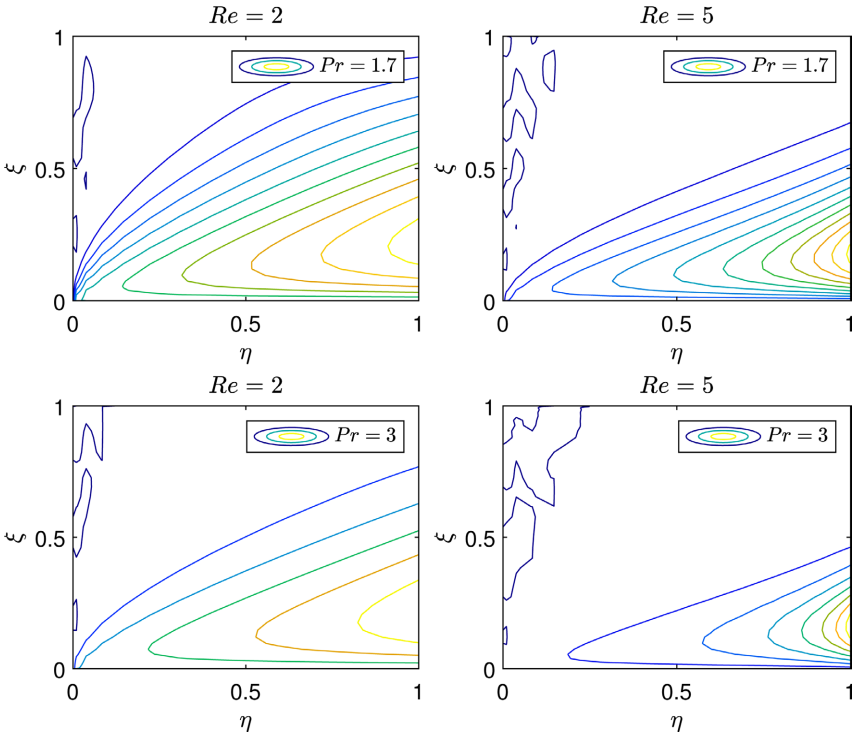

Figure 17. Temperature distribution for different values of *Re* and *Pr*.

Figure 20 and **Figure 21** are plotted to illustrate the impact of the Reynolds magnetic number on both x-axis magnetic field H_x and y-axis magnetic field H_z. From these figures we can see that as the Reynolds magnetic number, the

orientation and direction of the magnetic lines change from positive to negative or vice versa, see the first surface plot. The two separated groups of cells in the second contour plot are evidence of this. When the magnetic field is oriented in a

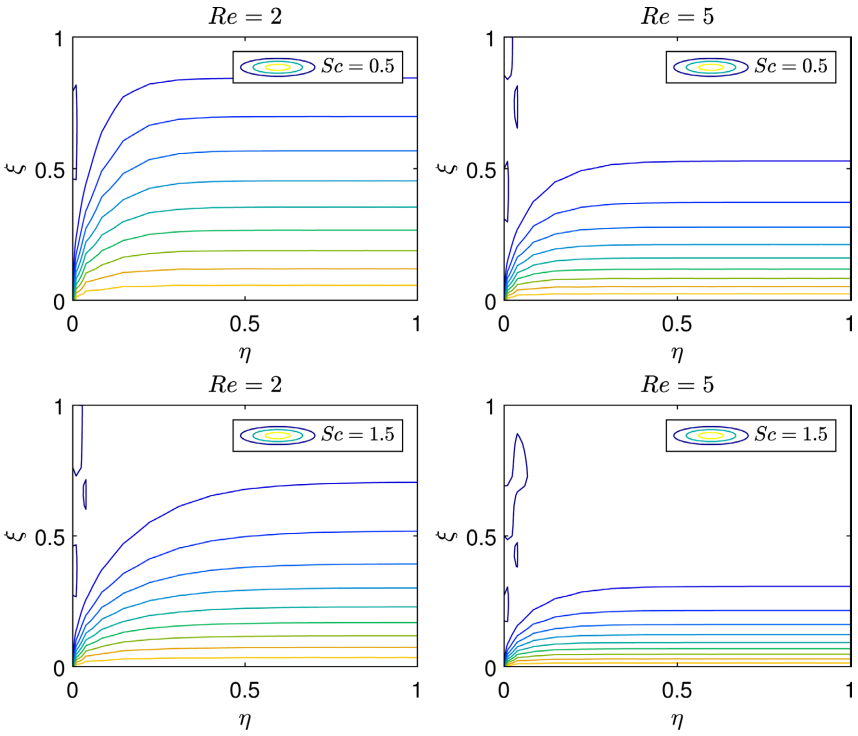

Figure 18. Concentration distribution for different values of *Re* and *Sc*.

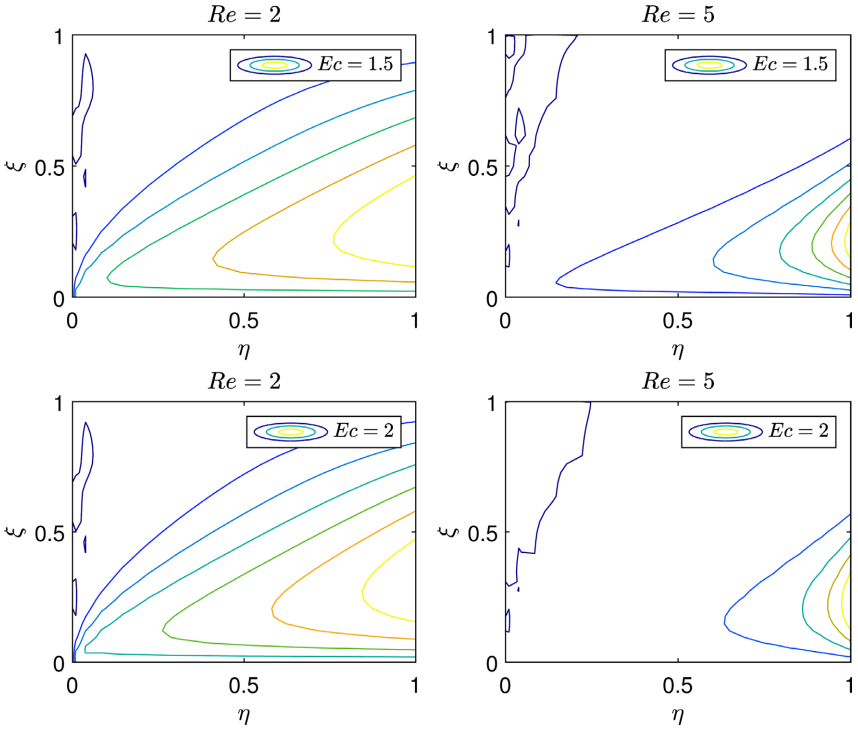

Figure 19. Temperature distribution for different values of *Re* and *Ec*.

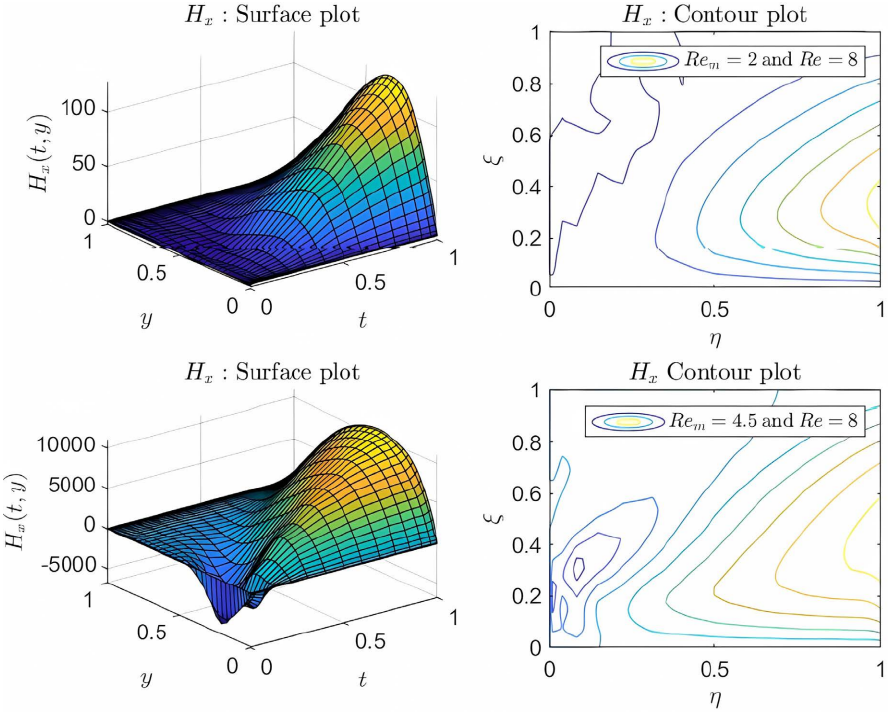

Figure 20. X-axis magnetic filed induction distribution for different values of *Re* and Re_m

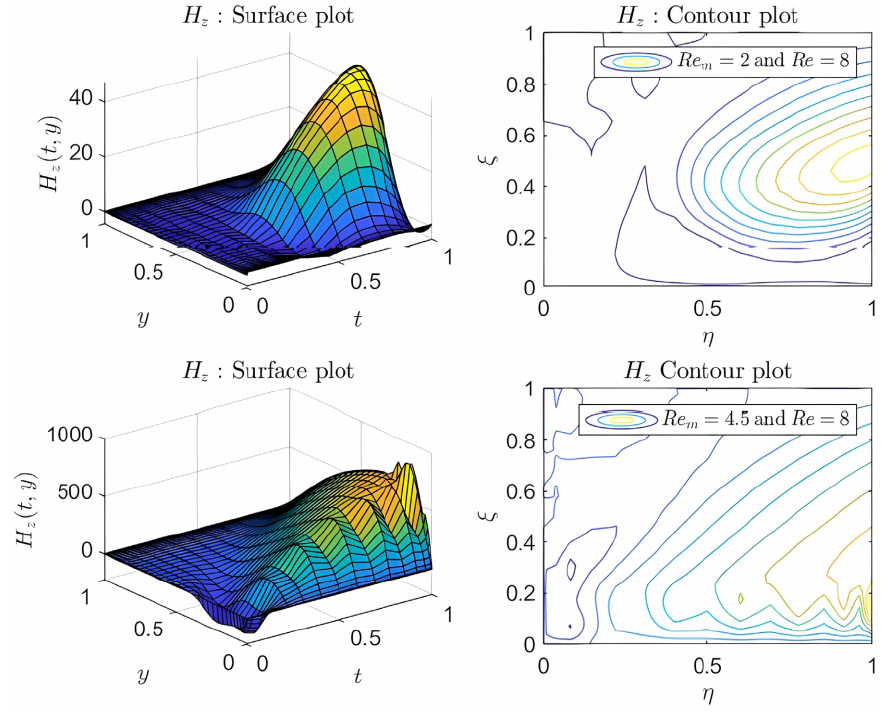

Figure 21. Z-axis magnetic filed induction distribution for different values of *Re* and Re_m

direction opposite to the normal vector of the domain by changing the magnetic polarity, the flux is negative, or when an arrangement of magnets takes place.

Table 2 and Table 3 display the primary and secondary skin friction under the influence of *M*, *K*, *Gr*, *Gm*, *R*, *Sc*, *Ec*, *Pr*, *Kc*, *Re*, and Re_m for various values of the

Table 2. Skin friction coefficient for primary velocity *u*.

M	K	Gr	Gm	R	Ec	Pr	Sc	Kc	Re	Re_m	$-C_{f,x}(\phi=0.35)$	$-C_{f,x}(\phi=0.4)$	$-C_{f,x}(\phi=0.45)$
10	0.5	10	10	1	0.5	1.7	0.5	1	0.5	0.5	4.3251	4.4641	4.7435
											4.8302	4.9784	5.2754
											5.3038	5.4617	5.7763
	1										4.2670	4.3968	4.6637
	1.5										4.2082	4.3287	4.5829
		15									4.0050	4.1769	4.4831
		20									3.6748	3.8826	4.2177
			15								2.9961	3.0720	3.2836
			20								1.6214	1.6329	1.7755
				2							4.3351	4.4749	4.7541
				3							4.3701	4.5122	4.7922
					1						4.0937	4.2121	4.4572
					1.5						3.8952	3.9971	4.2153
						3					4.0543	4.1754	4.4241
						4					3.8767	3.9834	4.2104
							1				4.3400	4.4801	4.7607
							1.5				4.3545	4.4958	4.7776
								2			4.3397	4.4799	4.7604
								3			4.3540	4.4952	4.7770
									1		2.8157	2.9008	3.0787
									1.5		2.1457	2.2164	2.3607
										1	4.1546	4.2765	4.5344
										1.5	4.0186	4.1321	4.3792

Table 3. Skin friction coefficient for secondary velocity *w*.

M	K	Gr	Gm	R	Ec	Pr	Sc	Kc	Re	Re_m	$C_{f,z}(\phi=0.35)$	$C_{f,z}(\phi=0.4)$	$C_{f,z}(\phi=0.45)$
10	0.5	10	10	1	0.5	1.7	0.5	1	0.5	0.5	2.7835	2.8359	2.9276
											2.8552	2.9123	3.0114
											2.9255	2.9869	3.0928
	1										2.8016	2.8563	2.9507
	1.5										2.8201	2.8770	2.9743
		15									2.8559	2.8993	2.9833
		20									2.9314	2.9649	3.0406
			15								3.0405	3.0965	3.1901

Continued

20								3.3038	3.3632	3.4589
	2							3.1750	3.2497	3.3655
	3							3.5540	3.6504	3.7901
		1						2.8029	2.8539	2.9444
		1.5						2.8231	2.8730	2.9624
			3					2.8022	2.8520	2.9409
			4					2.8138	2.8624	2.9497
				1				2.7788	2.8310	2.9225
				1.5				2.7742	2.8263	2.9175
					2			2.7789	2.8312	2.9227
					3			2.7745	2.8266	2.918
						1		2.1384	2.1875	2.2688
						1.5		1.8064	1.8479	1.9173
							1	2.7337	2.7747	2.8518
							1.5	2.6694	2.7028	2.7702

nanoparticle mass fraction. From **Table 2**, it is clear that increases in M, R, Sc, and Kc have been found to enhance the primary skin friction. On the other hand, the Primary skin friction reduces with increases in K, Gr, Gm, Ec, Pr, Re, and Re_m. Secondary skin friction is enhanced by increases in M, K, Gr, Gm, R, Ec and Pr while it is diminished by increases in Sc, Kc, Re, and Re_m. It is also observed that both the primary and secondary skin friction coefficient increases with an increase in the nanoparticle mass fraction ϕ. **Table 2** and **Table 3** represent the skin friction for various leading parameter variations. This involved setting up the values $R = 1$, $K = 0.5$, $Gr = 10$, $Gm = 10$, $M = 10$, $Pr = 0.71$, $Sc = 0.5$, $Je = 2$, $Kc = 1$, $Re_m = 0.5$, and $Re = 0.5$ which were then scattered around the range for computing reasons.

5. Conclusion

In this investigation, we carried out attributes of the convective flow of nanofluid flow with a vertical rotating plate imbedded in a porous medium by incorporating-induced magnetic field influence. The current model of the flow is utilized to stimulate the physical phenomena of the flow that occur inside the washing machine of the new generation, which is one of the frequent engineering utilizations in designing engineering products. The findings acquired are crucial in improving the performance of the new generation washing machine by adjusting the physical parameter values to get the best performance out of it. This paper uses the BI-SRM technique to numerically examine the effects of temperature-dependent viscosity, an induced magnetic field, nanofluid natural convection flow with heat and mass transfer, and a first-order chemical reaction through a semi-infinite, vertical

rotating plate embedded in a porous media. Analysis of the momentum equations and induction equations, which incorporate variable viscosity and variable magnetic field, is the major objective. The problem investigates the primary physical parameters, which are then utilized in the governing equations. The most significant engineering outcomes are highlighted and well explained. The key findings of the current research lead to the following significant conclusions:

- In case of varying the nanoparticle volume fraction, increases in *Gr*, *Gm*, *K*, and *Re* cause both the velocity components to accelerate, whereas increases in *M*, *Kc*, and *Sc* cause both velocity components to slow down.
- An increase in *Re* causes a reduction in fluid temperature, while *Re* has a reverse tendency in the concentration profile.
- Primary velocity slowed when *R* was raised and accelerated when Re_m was increased.
- Primary velocity increased when *Pr* increased in cases of low nanoparticle volume fraction concentration, but had the opposite tendency in cases of high nanoparticle volume fraction concentration.
- Secondary velocity accelerates with an increase in *R*, whilst an increase of Re_m decelerates the secondary velocity.
- The axial components of the induced magnetic field decline as Re_m increases.
- When *M*, *R*, *Sc*, and *Kc* increase, primary skin friction $C_{f,x}$ increases, but when *K*, *Gr*, *Gm*, *Ec*, *Pr*, *Re*, and Re_m increase, $C_{f,x}$ decrease.
- Increases in *M*, *K*, *Gr*, *Gm*, *R*, *Ec*, and *Pr* were linked to increased secondary skin friction $C_{f,z}$, whereas increases in *Sc*, *Kc*, *Re*, and Re_m were linked to decreased secondary skin friction $C_{f,z}$.
- In both primary and secondary velocities, an increase in nanoparticle volume fraction ϕ tends to increase skin friction.

In terms of future study, the authors recommend incorporating cross-diffusion effects, which are common in many real applications. Entropy generation analysis may also be used to improve the thermodynamic optimization of the model's system.

Data Availability

All required data is available in the text of the paper.

Acknowledgments

The African Union and the Pan African University's Institute for Basic Sciences, Technology, and Innovation (PAUSTI) were responsible for supporting this work, which the first author would like to acknowledge.

Conflicts of Interest

The authors declare no conflicts of interest regarding the publication of this paper.

References

[1] Masuda, H., Ebata, A., Teramae, K. and Hishinuma, N. (1993) Alteration of Thermal

Conductivity and Viscosity of Liquid by Dispersing Ultra-Fine Particles. Dispersion of Al_2O_3, SiO_2 and TiO_2 Ultra-Fine Particles. *Netsu Bussei*, **7**, 227-233. https://doi.org/10.2963/jjtp.7.227

[2] Choi, S. and Eastman, J.A. (1995) Enhancing Thermal Conductivity of Fluids with Nanoparticles. No. ANL/MSD/CP-84938; CONF-951135-29. Argonne National Lab (ANL), Argonne.

[3] Kakaç, S. and Pramuanjaroenkij, A. (2009) Review of Convective Heat Transfer Enhancement with Nanofluids. *International Journal of Heat and Mass Transfer*, **52**, 3187-3196. https://doi.org/10.1016/j.ijheatmasstransfer.2009.02.006

[4] Stephen, C., Zhang, Z.G. and Keblinski, P. (2004) Nanofluids. In Nalwa, H.S., Ed., *Encyclopedia of Nanoscience and Nanotechnology*, *vol.* 6, American Scientific Publishers, 757-773.

[5] Trisaksri, V. and Wongwises, S. (2007) Critical Review of Heat Transfer Characteristics of Nanofluids. *Renewable and Sustainable Energy Reviews*, **11**, 512-523. https://doi.org/10.1016/j.rser.2005.01.010

[6] Liu, M., Ching-Cheng Lin, M., Huang, I. and Wang, C. (2005) Enhancement of Thermal Conductivity with Carbon Nanotube for Nanofluids. *International Communications in Heat and Mass Transfer*, **32**, 1202-1210. https://doi.org/10.1016/j.icheatmasstransfer.2005.05.005

[7] Das, S.K., Choi, S.U.S. and Patel, H.E. (2006) Heat Transfer in Nanofluids—A Review. *Heat Transfer Engineering*, **27**, 3-19. https://doi.org/10.1080/01457630600904593

[8] Tyler, T., Shenderova, O., Cunningham, G., Walsh, J., Drobnik, J. and McGuire, G. (2006) Thermal Transport Properties of Diamond-Based Nanofluids and Nanocomposites. *Diamond and Related Materials*, **15**, 2078-2081. https://doi.org/10.1016/j.diamond.2006.08.007

[9] Yu, W., France, D.M., Routbort, J.L. and Choi, S.U.S. (2008) Review and Comparison of Nanofluid Thermal Conductivity and Heat Transfer Enhancements. *Heat Transfer Engineering*, **29**, 432-460. https://doi.org/10.1080/01457630701850851

[10] Choi, S.U.S. (2009) Nanofluids: From Vision to Reality through Research. *Journal of Heat Transfer*, **131**, Article 033106. https://doi.org/10.1115/1.3056479

[11] Salem, A.M. (2013) The Effects of Variable Viscosity, Viscous Dissipation and Chemical Reaction on Heat and Mass Transfer Flow of MHD Micropolar Fluid along a Permeable Stretching Sheet in a Non-Darcian Porous Medium. *Mathematical Problems in Engineering*, **2013**, Article 185074. https://doi.org/10.1155/2013/185074

[12] Hamad, M.A.A. and Pop, I. (2011) Unsteady MHD Free Convection Flow Past a Vertical Permeable Flat Plate in a Rotating Frame of Reference with Constant Heat Source in a Nanofluid. *Heat and Mass Transfer*, **47**, 1517-1524. https://doi.org/10.1007/s00231-011-0816-6

[13] Loganathan, P. and Sangeetha, S. (2022) Effect of Williamson Parameter on Cu-Water Williamson Nanofluid over a Vertical Plate. *International Communications in Heat and Mass Transfer*, **137**, Article 106273. https://doi.org/10.1016/j.icheatmasstransfer.2022.106273

[14] Ullah, H., Fiza, M., Khan, K., Batool, S., Ghufran, S.M. and Al-Mekhlafi, S.M. (2022) Effect of Joule Heating and Thermal Radiation of MHD Boundary Layer Oldroyd-B Nanofluid Flow with Heat Transfer over a Porous Stretching Sheet by Finite Element Method. *Journal of Nanomaterials*, **2022**, Article 7373631. https://doi.org/10.1155/2022/7373631

[15] Krishna, M.V. and Chamkha, A.J. (2020) Hall and Ion Slip Effects on Unsteady MHD Convective Rotating Flow of Nanofluids—Application in Biomedical Engineering. *Journal of the Egyptian Mathematical Society*, **28**, Article No. 1. https://doi.org/10.1186/s42787-019-0065-2

[16] Veera Krishna, M. and Chamkha, A.J. (2019) Hall and Ion Slip Effects on MHD Rotating Boundary Layer Flow of Nanofluid Past an Infinite Vertical Plate Embedded in a Porous Medium. *Results in Physics*, **15**, Article 102652. https://doi.org/10.1016/j.rinp.2019.102652

[17] Riasat, S., Ramzan, M., Kadry, S. and Chu, Y. (2020) Significance of Magnetic Reynolds Number in a Three-Dimensional Squeezing Darcy-Forchheimer Hydromagnetic Nanofluid Thin-Film Flow between Two Rotating Disks. *Scientific Reports*, **10**, Article No. 17208. https://doi.org/10.1038/s41598-020-74142-5

[18] Maneengam, A., Bouzennada, T., Abderrahmane, A., Guedri, K., Weera, W., Younis, O., *et al.* (2022) Numerical Study of Lid-Driven Hybrid Nanofluid Flow in a Corrugated Porous Cavity in the Presence of Magnetic Field. *Nanomaterials*, **12**, Article 2390. https://doi.org/10.3390/nano12142390

[19] Abumandour, R., Eldesoky, I.M., Abumandour, M., Morsy, K. and Ahmed, M.M. (2022) Magnetic Field Effects on Thermal Nanofluid Flowing through Vertical Stenotic Artery: Analytical Study. *Mathematics*, **10**, Article 492. https://doi.org/10.3390/math10030492

[20] Ur Rasheed, H., AL-Zubaidi, A., Islam, S., Saleem, S., Khan, Z. and Khan, W. (2021) Effects of Joule Heating and Viscous Dissipation on Magnetohydrodynamic Boundary Layer Flow of Jeffrey Nanofluid over a Vertically Stretching Cylinder. *Coatings*, **11**, Article 353. https://doi.org/10.3390/coatings11030353

[21] Hossain, S.M.C., Ferdows, M., Bangalee, M.Z.I. and Alam, M.S. (2022) Two-Phase Bio-Nanofluid Flow through a Bifurcated Artery with Magnetic Field Interaction. *International Journal of Thermofluids*, **15**, Article 100194. https://doi.org/10.1016/j.ijft.2022.100194

[22] Mandal, G. (2016) Convective-Radiative Heat Transfer of Micropolar Nanofluid over a Vertical Non-Linear Stretching Sheet. *Journal of Nanofluids*, **5**, 852-860. https://doi.org/10.1166/jon.2016.1265

[23] Pal, D. and Mandal, G. (2017) Thermal Radiation and MHD Effects on Boundary Layer Flow of Micropolar Nanofluid Past a Stretching Sheet with Non-Uniform Heat Source/Sink. *International Journal of Mechanical Sciences*, **126**, 308-318. https://doi.org/10.1016/j.ijmecsci.2016.12.023

[24] Pal, D. and Mandal, G. (2023) Stability Analysis and Implication of Darcy Magnetic-Radiative Hybrid Reactive Nanofluid Heat Transfer over a Shrinkable Surface with Ohmic Heating. *Journal of Thermal Analysis and Calorimetry*, **148**, 2087-2104. https://doi.org/10.1007/s10973-022-11797-4

[25] Pal, D. and Mandal, G. (2021) Magnetohydrodynamic Nonlinear Thermal Radiative Heat Transfer of Nanofluids Over a Flat Plate in a Porous Medium in Existence of Variable Thermal Conductivity and Chemical Reaction. *International Journal of Ambient Energy*, **42**, 1167-1177.

[26] Mulinti, V.R. and Pallavarapu, L. (2021) Influence of Thermal Radiation and Viscous Dissipation on MHD Flow of UCM Fluid over a Porous Stretching Sheet with Higher Order Chemical Reaction. *Special Topics & Reviews in Porous Media*, **12**, 33-49. https://doi.org/10.1615/specialtopicsrevporousmedia.2020033950

[27] Vinodkumar Reddy, M., Sucharitha, G., Vajravelu, K. and Lakshminarayana, P. (2022) Convective Flow of MHD Non-Newtonian Nanofluids on a Chemically

Reacting Porous Sheet with Cattaneo-Christov Double Diffusion. *Waves in Random and Complex Media*, 1-20. https://doi.org/10.1080/17455030.2022.2111478

[28] Vinodkumar Reddy, M. and Lakshminarayana, P. (2022) Higher Order Chemical Reaction and Radiation Effects on Magnetohydrodynamic Flow of a Maxwell Nanofluid with Cattaneo-Christov Heat Flux Model over a Stretching Sheet in a Porous Medium. *Journal of Fluids Engineering*, **144**, Article 041204. https://doi.org/10.1115/1.4053250

[29] Meenakumari, R., Lakshminarayana, P. and Vajravelu, K. (2021) Unsteady MHD Flow of a Williamson Nanofluid on a Permeable Stretching Surface with Radiation and Chemical Reaction Effects. *The European Physical Journal Special Topics*, **230**, 1355-1370. https://doi.org/10.1140/epjs/s11734-021-00039-7

[30] Reddy, J.V.R., Sugunamma, V., Sandeep, N. and Sulochana, C. (2016) Influence of Chemical Reaction, Radiation and Rotation on MHD Nanofluid Flow Past a Permeable Flat Plate in Porous Medium. *Journal of the Nigerian Mathematical Society*, **35**, 48-65. https://doi.org/10.1016/j.jnnms.2015.08.004

[31] Kumar, R. and Sood, S. (2017) Combined Influence of Fluctuations in the Temperature and Stretching Velocity of the Sheet on MHD Flow of Cu-Water Nanofluid through Rotating Porous Medium with Cubic Auto-Catalysis Chemical Reaction. *Journal of Molecular Liquids*, **237**, 347-360. https://doi.org/10.1016/j.molliq.2017.04.054

[32] Reddy, P.S., Sreedevi, P. and Chamkha, A.J. (2017) MHD Boundary Layer Flow, Heat and Mass Transfer Analysis over a Rotating Disk through Porous Medium Saturated by Cu-Water and Ag-Water Nanofluid with Chemical Reaction. *Powder Technology*, **307**, 46-55. https://doi.org/10.1016/j.powtec.2016.11.017

[33] Rashid, A., Ayaz, M. and Islam, S. (2023) Mixed Convection MHD Hybrid Nanofluid Flow between Two Parallel Rotating Discs with Joule Heating and Chemical Reactions Using bvp4c. *Advances in Mechanical Engineering*, **15**. https://doi.org/10.1177/16878132231179611

[34] Abd-Alla, A.M., Abo-Dahab, S.M., Thabet, E.N., Bayones, F.S. and Abdelhafez, M.A. (2023) Heat and Mass Transfer in a Peristaltic Rotating Frame Jeffrey Fluid via Porous Medium with Chemical Reaction and Wall Properties. *Alexandria Engineering Journal*, **66**, 405-420. https://doi.org/10.1016/j.aej.2022.11.016

[35] Sharma, P.L., Kapalta, M., Kumar, A., Bains, D., Gupta, S. and Thakur, P. (2023) Electrohydro Dynamics Convection in Dielectric Rotating Oldroydian Nanofluid in Porous Medium. *Journal of the Nigerian Society of Physical Sciences*, **5**, Article 1231. https://doi.org/10.46481/jnsps.2023.1231

[36] Umavathi, J.C., Bég, O.A., Khan, U.F., Bég, T.A. and Kadir, A. (2023) Computation of Swirling Hydromagnetic Nanofluid Flow Containing Gyrotactic Microorganisms from a Spinning Disk to a Porous Medium with Hall Current and Anisotropic Slip Effects. *ZAMM-Journal of Applied Mathematics and Mechanics/Zeitschrift für Angewandte Mathematik und Mechanik*, **103**, e202100575. https://doi.org/10.1002/zamm.202100575

[37] Qayyum, M., Afzal, S., Ali, M.R., Sohail, M., Imran, N. and Chambashi, G. (2023) Unsteady Hybrid Nanofluid (UO_2, MWCNTs/Blood) Flow between Two Rotating Stretchable Disks with Chemical Reaction and Activation Energy under the Influence of Convective Boundaries. *Scientific Reports*, **13**, Article No. 6151. https://doi.org/10.1038/s41598-023-32606-4

[38] Krishna, M.V. and Chamkha, A.J. (2023) Hall and Ion Slip Impacts on Unsteady MHD Convective Flow of Ag-TiO_2/WEG Hybrid Nanofluid in a Rotating Frame.

Current Nanoscience, **19**, 15-32.
https://doi.org/10.2174/1573413717666211018113823

[39] Ahmad, B., Saeed, M., Mahmood Ul-Hassan, Q., Abbas, T. and Mehmood, M. (2023) Mechanism of Hydrodynamic Viscosity Variation and Convective Boundary for Flow of Micropolar Nanofluid within Porous Medium. *Waves in Random and Complex Media*, 1-31. https://doi.org/10.1080/17455030.2023.2190811

[40] Puneeth, V., Aly, E.H. and Pop, I. (2023) Nanofluid Flowing over a Rotating Disk That Is Stretching and Permeable: An Unsteady Model. *International Journal of Modern Physics B*, **37**, Article 2350249. https://doi.org/10.1142/s0217979223502491

[41] Raghunath, K. (2023) Study of Heat and Mass Transfer of an Unsteady Magnetohydrodynamic (MHD) Nanofluid Flow Past a Vertical Porous Plate in the Presence of Chemical Reaction, Radiation and Soret Effects. *Journal of Nanofluids*, **12**, 767-776. https://doi.org/10.1166/jon.2023.1965

[42] Sekhar, B.C. and Kumar, P.V. (2022) Thermodiffusion and Chemical Reaction on MHD Free Convective Flow Past a Rotating Vertical Porous Plate with Constant Heat and Mass Discharge. *Heat Transfer*, **51**, 3142-3165. https://doi.org/10.1002/htj.22441

[43] Veera Krishna, M., Ameer Ahamad, N. and Chamkha, A.J. (2021) Hall and Ion Slip Impacts on Unsteady MHD Convective Rotating Flow of Heat Generating/Absorbing Second Grade Fluid. *Alexandria Engineering Journal*, **60**, 845-858.
https://doi.org/10.1016/j.aej.2020.10.013

[44] Veera Krishna, M., Ameer Ahamad, N. and Aljohani, A.F. (2021) Thermal Radiation, Chemical Reaction, Hall and Ion Slip Effects on MHD Oscillatory Rotating Flow of Micro-Polar Liquid. *Alexandria Engineering Journal*, **60**, 3467-3484.
https://doi.org/10.1016/j.aej.2021.02.013

[45] Sehra, Haq, S.U., Shah, S.I.A., Nisar, K.S., Jan, S.U. and Khan, I. (2021) Convection Heat Mass Transfer and MHD Flow over a Vertical Plate with Chemical Reaction, Arbitrary Shear Stress and Exponential Heating. *Scientific Reports*, **11**, Article No. 4265. https://doi.org/10.1038/s41598-021-81615-8

[46] Raghunath, K., Ganteda, C. and Lorenzini, G. (2022) Effects of Soret, Rotation, Hall, and Ion Slip on Unsteady MHD Flow of a Jeffrey Fluid through a Porous Medium in the Presence of Heat Absorption and Chemical Reaction. *Journal of Mechanical Engineering Research and Developments*, **45**, 80-97.

[47] Krishna, M.V. (2022) Hall and Ion Slip Effects and Chemical Reaction on MHD Rotating Convective Flow Past an Infinite Vertical Porous Plate with Ramped Wall and Uniform Wall Temperatures. *Biomass Conversion and Biorefinery*, **14**, 11647-11664.
https://doi.org/10.1007/s13399-022-03160-2

[48] Krishna, M.V. and Vajravelu, K. (2022) Rotating MHD Flow of Second Grade Fluid through Porous Medium between Two Vertical Plates with Chemical Reaction, Radiation Absorption, Hall, and Ion Slip Impacts. *Biomass Conversion and Biorefinery*, **14**, 8745-8759. https://doi.org/10.1007/s13399-022-02802-9

[49] Prabhakar Reddy, B. and Makinde, O.D. (2021) Numerical Study on Heat Absorbing MHD Radiating and Reacting Flow Past an Impulsively Moving Vertical Plate with Ramped Temperature and Concentration with Hall Current. *International Journal for Computational Methods in Engineering Science and Mechanics*, **23**, 383-395.
https://doi.org/10.1080/15502287.2021.1977419

[50] Veera Krishna, M., Ahamad, N.A. and Chamkha, A.J. (2021) Numerical Investigation on Unsteady MHD Convective Rotating Flow Past an Infinite Vertical Moving Porous Surface. *Ain Shams Engineering Journal*, **12**, 2099-2109.
https://doi.org/10.1016/j.asej.2020.10.013

[51] Ayub, R., Ahmad, S. and Ahmad, M. (2022) MHD Rotational Flow of Viscous Fluid Past a Vertical Plate with Slip and Hall Effect through Porous Media: A Theoretical Modeling with Heat and Mass Transfer. *Advances in Mechanical Engineering*, **14**. https://doi.org/10.1177/16878132221103330

[52] Ali, B., Naqvi, R.A., Nie, Y., Khan, S.A., Sadiq, M.T., Rehman, A.U., *et al.* (2020) Variable Viscosity Effects on Unsteady MHD an Axisymmetric Nanofluid Flow over a Stretching Surface with Thermo-Diffusion: FEM Approach. *Symmetry*, **12**, Article 234. https://doi.org/10.3390/sym12020234

[53] Khan, M., Shahid, A., Salahuddin, T., Malik, M.Y. and Mushtaq, M. (2018) Heat and Mass Diffusions for Casson Nanofluid Flow over a Stretching Surface with Variable Viscosity and Convective Boundary Conditions. *Journal of the Brazilian Society of Mechanical Sciences and Engineering*, **40**, Article No. 533. https://doi.org/10.1007/s40430-018-1415-y

[54] Magagula, V.M., Motsa, S.S., Sibanda, P. and Dlamini, P.G. (2016) On a Bivariate Spectral Relaxation Method for Unsteady Magneto-Hydrodynamic Flow in Porous Media. *SpringerPlus*, **5**, Article No. 455. https://doi.org/10.1186/s40064-016-2053-4

[55] Rai, N. and Mondal, S. (2021) Spectral Methods to Solve Nonlinear Problems: A Review. *Partial Differential Equations in Applied Mathematics*, **4**, Article 100043. https://doi.org/10.1016/j.padiff.2021.100043

[56] Minea, A.A. (2019) A Review on Electrical Conductivity of Nanoparticle-Enhanced Fluids. *Nanomaterials*, **9**, Article 1592. https://doi.org/10.3390/nano9111592

[57] Lai, F.C. and Kulacki, F.A. (1990) The Effect of Variable Viscosity on Convective Heat Transfer along a Vertical Surface in a Saturated Porous Medium. *International Journal of Heat and Mass Transfer*, **33**, 1028-1031. https://doi.org/10.1016/0017-9310(90)90084-8

[58] Motsa, S.S., Dlamini, P.G. and Khumalo, M. (2014) Spectral Relaxation Method and Spectral Quasilinearization Method for Solving Unsteady Boundary Layer Flow Problems. *Advances in Mathematical Physics*, **2014**, Article 341964. https://doi.org/10.1155/2014/341964

[59] Trefethen, L.N. (2000) Spectral Methods in MATLAB. Society for Industrial and Applied Mathematics. https://doi.org/10.1137/1.9780898719598